Two-Dimensional Titanium Carbide (MXene) based Films: Expanding the Frontier of Functional Film Materials

Guohao Li, Brian C. Wyatt, Fei Song, Changqiang Yu, Zhenjun Wu, Xiuqiang Xie*, Babak Anasori*, Nan Zhang*

G. Li, F. Song, Dr. C. Yu, Prof. X. Xie and Prof. N. Zhang
College of Materials Science and Engineering, Hunan University, Changsha 410082, P. R. China.
E-mail: nanzhang@hnu.edu.cn; xiuqiang_xie@hnu.edu.cn.

B. C. Wyatt and Prof. B. Anasori
Department of Mechanical and Energy Engineering and Integrated Nanosystems Development Institute, Purdue School of Engineering and Technology, Indiana University–Purdue University Indianapolis, USA.
E-mail: banasori@iupui.edu.

Prof. Z. Wu
College of Chemistry and Chemical Engineering, Hunan University, Changsha 410082, P. R. China.

Two-dimensional (2D) titanium carbide (Ti$_3$C$_2$T$_x$) MXene films, with their well-defined microstructures and chemical functionality, provide a macroscale use of nano-sized Ti$_3$C$_2$T$_x$ flakes. Ti$_3$C$_2$T$_x$ films have attractive physicochemical properties favorable for device design, such as high electrical conductivity (up to 20,000 S cm^{-1}), impressive volumetric capacitance (1,500 F cm^{-3}), strong in-plane mechanical strength (up to 570 MPa), and high degree flexibility. Here, the appealing features of Ti$_3$C$_2$T$_x$-based films enabled by the layer-to-layer arrangement of nanosheets are reviewed. We devote attention to the key strategies for actualizing desirable characteristics in Ti$_3$C$_2$T$_x$-based functional films, such as high and tunable electrical conductivity, outstanding mechanical properties, enhanced oxidation-resistance and shelf life, hydrophilicity/hydrophobicity, adjustable porosity and convenient processability. This review further discusses fundamental aspects and advances in the applications of Ti$_3$C$_2$T$_x$-based films, with a focus on illuminating the relationship between the structural features and the resultant performances for target applications. Finally, the challenges and opportunities in terms of future

research, development, and applications of $Ti_3C_2T_x$-based films are suggested. A comprehensive understanding of these competitive features and challenges shall provide guidelines and inspiration for the further development of $Ti_3C_2T_x$-based functional films, and contribute to the advances in MXenes technologies.

1. Introduction

The past decades have witnessed some dramatic developments in the area of nanomaterials, which exhibit fascinating optical, electrical, and magnetic properties emerging at nanoscale.[1] These impressive properties have motivated the construction of functional devices using these nanomaterials toward practical applications.[2, 3] Film materials comprised of nanomaterials have gained considerable attention since they combine the fundamental nanoscience with feasible macroscale application, such as portable power supplies,[4] water purification,[5] and electromagnetic interference shielding.[6] With novel nanosized building blocks of film materials, more functionalities and improved device performances are expected, which drives the continuing growth of many modern technologies.

Since the discovery of graphene in 2004,[7] two-dimensional (2D) materials have been one of the research hotspots in materials science due to their unique 2D structure and outstanding physicochemical properties. In the past decade, there has been tremendous development in 2D materials in a variety of applications, which has enriched the research imagination of the community.[8, 9] One of the latest additions to the list of 2D materials are the family of transition metal carbides and/or nitrides (known as MXenes), which have driven an enormous amount of research interest since they were first reported by researchers at Drexel University in 2011.[10] 2D MXenes are typically generated from their corresponding 3D bulk MAX phase precursors via the selective etching of A-group element (generally groups 13-14 elements of the periodic table, most commonly Al) layers (**Figure 1a**).[11-14] The general formula of MXenes can be written as $M_{n+1}X_nT_x$ ($n = 1 - 4$), where M is an early transition metal (e.g., Ti, Zr, V, Nb, Ta, or Mo), X is carbon and/or nitrogen, and T_x represents the various surface functionalities, such as –(OH), =O, –F, and –Cl, which result from the etching process.[15-19] The structure of $Ti_3C_2T_x$ is shown in Figure 1b. Due to the unique structure and surface chemistry, MXenes possess metallic conductivity, excellent hydrophilicity, and good flexibility, which makes them the focus of researchers.[20-23]

3

So far, more than 20 different MXenes have been experimentally synthesized, including $Ti_3C_2T_x$,[24] Mo_2CT_x,[25] Ti_2CT_x,[26] $Nb_4C_3T_x$,[27] Nb_2CT_x,[28] V_2CT_x,[29] $Mo_2TiC_2T_x$,[30] $Mo_2Ti_2C_3T_x$.[31] Among various MXenes, $Ti_3C_2T_x$ is the most explored [17] due to its relatively high electrical conductivity (up to 20,000 S cm^{-1}, as compared in Figure 1c),[32] low ion diffusion barrier, negative surface charge in solutions (-40 mV in water),[33] low operating voltage,[34] mechanical flexibility,[23] and environmental friendliness,[35, 36] which have shown $Ti_3C_2T_x$'s promising potential for application in many fields, such as electromagnetic interference (EMI) shielding,[37] , wireless communications,[38] electrocatalytic hydrogen evolution,[39] piezoresistive sensor,[40] and separation membranes.[41] Especially, $Ti_3C_2T_x$ exhibits advantageous properties for electrochemical energy storage compared to many other 2D materials due to its high electrical conductivity, abundant surface functionalities, and incorporation potential of redox-active transition metals.[42-45] Furthermore, the ability to utilize these impressive electrochemical, mechanical, and optoelectronic properties in an assembled flexible freestanding film further expands their applications in flexible devices. For instance, freestanding, flexible $Ti_3C_2T_x$-based films can be directly used as electrodes without a metal current collector in energy storage applications, which is advantageous for wearable and portable devices where size matters.[46, 47] Xu *et al.* fabricated binder-free flexible $Ti_3C_2T_x$ electrodes for supercapacitors with stable cycling performance through a simple modified electrophoretic deposition.[48] The assembled flexible symmetric all-solid-state supercapacitor with two pieces of $Ti_3C_2T_x$ film on conductive fabric substrates exhibits good flexibility, which can be used to fabricate watchband-like supercapacitors capable of powering a LED.[48]

However, there are still several bottlenecks in $Ti_3C_2T_x$-based films synthesis and fabrication, including face-to-face compact restacking of $Ti_3C_2T_x$ nanosheets when flakes assemble into films, and unsatisfactory stability in oxygen-containing or humid atmospheres above room temperature conditions, which can lead to significant deterioration of the physicochemical properties and restrict its further use.[49, 50] To combat these effects, methods of surface

4

modification and structural design have been developed to enhance the performance of $Ti_3C_2T_x$-based films. In fact, inspired by the compelling successes of porous structure in alleviating the above challenges in other 2D materials,[51, 52] researchers have devoted great effort into the elaborate design of porous MXenes within the recent five years.[53] For example, Zhao *et al.* processed 2D $Ti_3C_2T_x$ flakes into 3D architectures via a simple sulfur-template method.[54] The $Ti_3C_2T_x$ films are freestanding, flexible, and highly conductive with open 3D macroporous structure and abundant active sites, which mitigates the self-restacking issue. As a result of this 3D macroporous structure, the obtained $Ti_3C_2T_x$ films exhibit an outstanding and stable capacity of 314.9 mA h g^{-1} at 50 mA g^{-1} after 300 cycles, which is almost four times higher than that of pure stacked $Ti_3C_2T_x$ films.[54]

Although research on $Ti_3C_2T_x$-based films continues to bring us significant technological advances, there are some existing challenges to overcome in the application of these wondrous materials. In this review, we first provide an overview of the competitive features of $Ti_3C_2T_x$-based films, followed by an introduction of their important figure-of-merits and the engineering strategies. Finally, we summarize the applications of $Ti_3C_2T_x$-films, which include lithium/sodium-ion storage, (micro-)supercapacitors, transparent conductive electrodes, water purification, and other applications. In this review, we provide a special focus on the importance of compositions and structures in the modification of MXenes properties toward target applications (Figure 1d).[55]
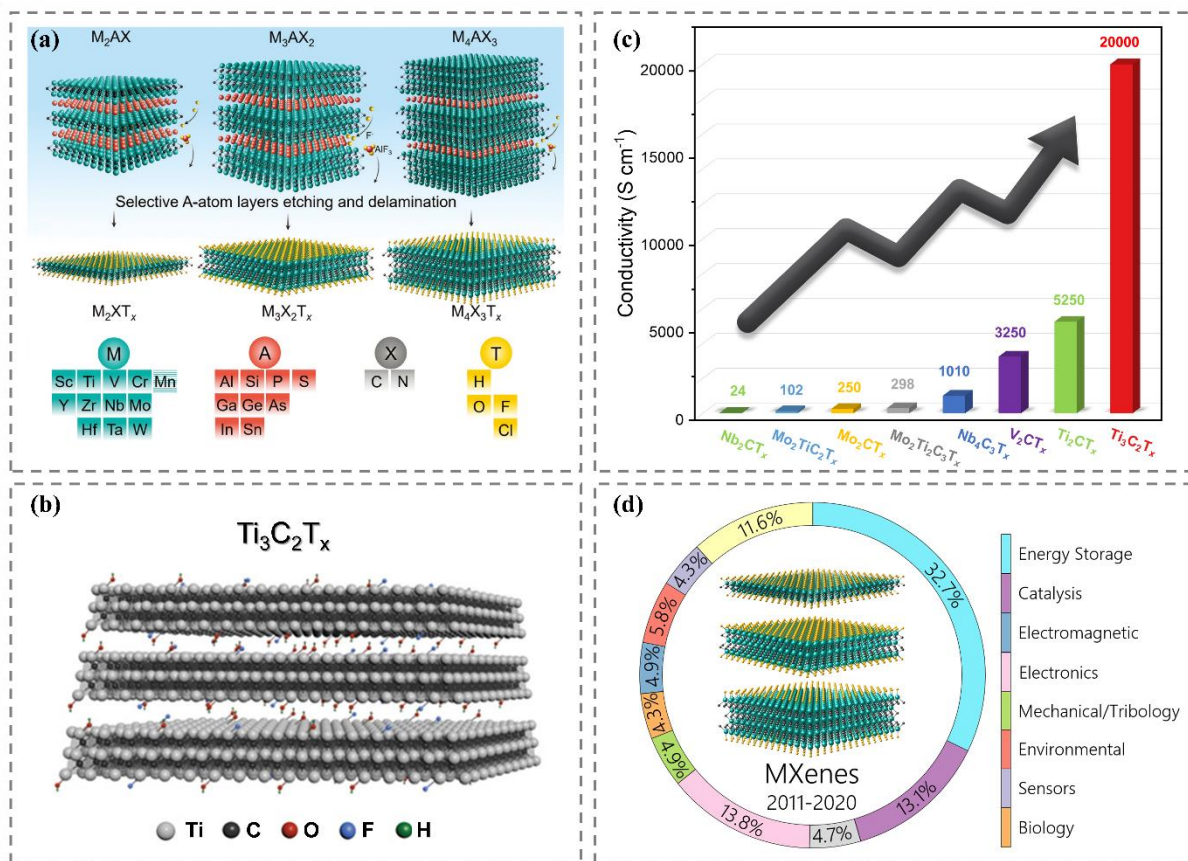
Figure 1. (a) General schematic illustration of the formation of MXenes from the corresponding parent MAX-phase. Reproduced with permission.[55] Copyright 2021, Wiley. (b) The molecular structure model of single-layer $Ti_3C_2T_x$. Reproduced with permission.[56] Copyright 2019, Wiley. (c) The electrical conductivity comparison of $Ti_3C_2T_x$,[32] Mo_2CT_x,[57] Ti_2CT_x,[58] $Nb_4C_3T_x$,[59] Nb_2CT_x,[60] V_2CT_x,[61] $Mo_2TiC_2T_x$ and $Mo_2Ti_2C_3T_x$.[62] (d) Applications of MXenes in different areas.[55]

2. Competitive features of $Ti_3C_2T_x$ MXene-based films and methods to enhance them

$Ti_3C_2T_x$ nanosheets suspended in water-based colloidal solutions are very stable due to MXene flakes' excellent hydrophilic surface and electrostatic repulsion between neighboring nanosheets. These properties make $Ti_3C_2T_x$ an easy nanomaterial to fabricate films by vacuum filtration or spray coating. $Ti_3C_2T_x$-based films possess a lot of advantages such as its high and tunable electrical conductivity, outstanding mechanical properties, enhanced oxidation-resistance and shelf life[32, 63], hydrophilicity/hydrophobicity, adjustable porosity and convenient processability (**Figure 2**), which will be the focus of this section. For example, even with abundant surface active groups (–(OH), =O, and –F), $Ti_3C_2T_x$-based films exhibit superior

electrical conductivity.[64, 65] Although the electrochemical performance of $Ti_3C_2T_x$-based films is still restricted by the restacking of $Ti_3C_2T_x$ nanosheets via van der Waals interactions and hydrogen bonds, the performance optimization through the design of microstructures has demonstrated the great promise of $Ti_3C_2T_x$-based films for a broad spectrum of applications. For example, $Ti_3C_2T_x$-based films demonstrated promising rate capability and volumetric capacitance for electrochemical energy storage.[66, 67] As for the optoelectronic properties, $Ti_3C_2T_x$ (colloidal aggregate-flakes) show great figure of merit twice as large as reduced graphene oxide (rGO) (3.1 *vs.* 1.6).[68]

Figure 2. Competitive features of titanium carbide (MXene)-based films.

In addition, we also introduce some effective methods to optimize the above features in this section, such as controlling the size and defects of $Ti_3C_2T_x$ flakes, doping, and templating (**Table 1**), which would be useful for researchers to design advanced $Ti_3C_2T_x$-based films for diverse applications.

Table 1. Summarized modification methods to improve different properties of $Ti_3C_2T_x$-based films

| Film Materials	Target	Controlled factor	Strategy	Ref.
$Ti_3C_2T_x$	Conductivity enhancement	Using larger $Ti_3C_2T_x$ flakes with few defects	Minimally intensive layer delamination	[62]
$Ti_3C_2T_x$	Conductivity and flexibility enhancement	Using $Ti_3C_2T_x$ flakes with high aspect ratio and highly aligned films	Preselecting large MAX precursor and blade-coating	[69]
$Ti_3C_2T_x$	Conductivity enhancement	Reducing defects in the surface Ti layer	Using modified MAX precursor	[32]
$Ti_3C_2T_x$, Ti_3CNT_x, $Mo_2TiC_2T_x$	Conductivity enhancement	Removing structural water and surface groups	Annealing	[65]
$Ti_3C_2T_x$ + HCl + $HClO_4$	Conductivity and oxidation-resistance enhancement	Desorption of Li^+	Acid treatment	[70]
$Ti_3C_2T_x$, K^+, Al^{3+}	Mechanical property enhancement	Formation of ionic bonds	Introduction of metal ions	[71, 72]
$Ti_3C_2T_x$ + PDDA, $Ti_3C_2T_x$ + Cellulose Nanofibers	Mechanical property enhancement	Formation of bonds and synergistic effect	Polymer addition	[33, 73]
$Ti_3C_2T_x$ + rGO	Mechanical property enhancement	Formation of covalent bonds	Nanomaterial doping	[74]
$Ti_3C_2T_x$	Oxidation-resistance enhancement	Formation of protective shells for the interior flakes	Thick film	[68]
$Ti_3C_2T_x$ + (P(VDF-TrFE))	Oxidation-resistance enhancement	Formation of hydrophobic shells	Hydrophobic polymer addition	[3]
$Ti_3C_2T_x$ + Natural Rubber	Shelf life enhancement	Formation of strong bonds and reliable shells	Polymer addition	[75]
$Ti_3C_2T_{x=}$ + Aramid Nanofiber	Shelf life enhancement	Formation of strong hydrogen bonds	Polymer addition	[76]
$Ti_3C_2T_x$ + rGO	Hydrophilicity enhancement	Increasing the proportion of –OH	HCl treatment	[77]
$Ti_3C_2T_x$ + Hydrazine Monohydrate	Hydrophilicity to hydrophobicity transformation	Reaction between Ti–OH with hydrazine	Hydrazine treatment	[78]
$Ti_3C_2T_x$ + sulfur, $Ti_3C_2T_x$	Porous structure	Using ice/sulfur as the templates	Hard templating	[54, 79]
$Ti_3C_2T_x$	Conductivity enhancement	Using larger $Ti_3C_2T_x$ flakes with few defects	Minimally intensive layer delamination	[62]
$Ti_3C_2T_x$	Conductivity and flexibility enhancement	Using $Ti_3C_2T_x$ flakes with high aspect ratio and highly aligned films	Preselecting large MAX precursor and blade-coating	[69]

2.1. High and tunable electrical conductivity

High electrical conductivity is critical to obtain an improved performance toward applications in flexible electronics, such as supercapacitors, EMI shielding, antennas, sensors, and actuators. Compared to that of the 2D analogue of rGO, one of the most prominent properties of $Ti_3C_2T_x$-based films is the high electrical conductivity, which is favorable for the rapid transfer of electrons during the charge/discharge process to ensure high power delivery in energy storage devices.[82] For example, it has been found by Ma *et al.* that the conductivity of $Ti_3C_2T_x$ film used in their study (2,863 S cm^{-1}) is three orders of magnitude higher than that of rGO film (1.64 S cm^{-1}). The superior electrical conductivity of $Ti_3C_2T_x$ film is evidenced by the electrochemical impedance of $Ti_3C_2T_x$, rGO, and hybridized $Ti_3C_2T_x$/rGO films shown in **Figure 3**a.[83] Noteworthily, the electrical conductivity varies with the synthetic protocols for both $Ti_3C_2T_x$ and rGO. The highest electrical conductivity value reported of $Ti_3C_2T_x$ is up to 20,000 S cm^{-1},[32] which is about 3.2 times higher than the highest value reported for rGO (6,300 S cm^{-1}).[84] This value also exceeds the highest one reported for the film of graphene with minimal topological defects (17,300 S cm^{-1}),[85] as compared in Figure 3b. It has been revealed that the electrical conductivity of $Ti_3C_2T_x$ is significantly influenced by its morphological and structural characteristics.[86] In general, a low concentration of defects and large flake size result in higher conductivity,[87] which means a milder etchant (compared to HF) and minimally intensive layer delamination (MILD) may be an optimal synthesis method of $Ti_3C_2T_x$ for higher conductivity. The MILD method for selectively etching the Ti_3AlC_2 precursor uses an increased molar ratio of LiF to Ti_3AlC_2 from 5:1[88] to 7.5:1, followed by a simple manual shaking step (instead of sonication) for the delamination of multilayered $Ti_3C_2T_x$.[62, 86] The $Ti_3C_2T_x$ flakes made by the improved method is large (up to 15 µm) and visually hole-free with well-defined and clean edges. As a result, the electrical conductivity of $Ti_3C_2T_x$ flakes made by the improved method were measured to be 4,600 ± 1,100 S cm^{-1}, while that made by original direct use of HF method was about 1,500 S cm^{-1}.[88] When the $Ti_3C_2T_x$ flakes made by the MILD method

were filtered to form a MXene film, the electrical conductivity was measured to be ~ 4,600 S cm^{-1} as well.[62] In addition to the improved MXene etching routes, Zhang *et al.* fabricated high aspect ratio $Ti_3C_2T_x$ flakes through preselecting the large corresponding MAX phase and then adjusting the etching conditions (Figure 3c).[69] In this study, they used a blade-coating method to fabricate large area $Ti_3C_2T_x$ films containing highly aligned $Ti_3C_2T_x$ flakes, which can further improve the conductivity due to the highly densified stacking and alignment of $Ti_3C_2T_x$ layers. The resulting $Ti_3C_2T_x$ film achieved a value of $15,100 \pm 160$ S cm^{-1}, which is higher than their control $Ti_3C_2T_x$ film produced by vacuum-assisted filtration (Figure 3d).[69] In addition, recent studies have shown that the Ti_3AlC_2 MAX precursor synthesis process greatly affects the electrical conductivity of the resultant $Ti_3C_2T_x$ film. For example, it was shown that excess Al inclusion in Ti_3AlC_2 synthesis minimizes defects in the surface Ti layer of $Ti_3C_2T_x$ after hydrofluoric acid etching, which resulted in the current record of 20,000 S cm^{-1} electrical conductivity of a vacuum filtered film.[32]
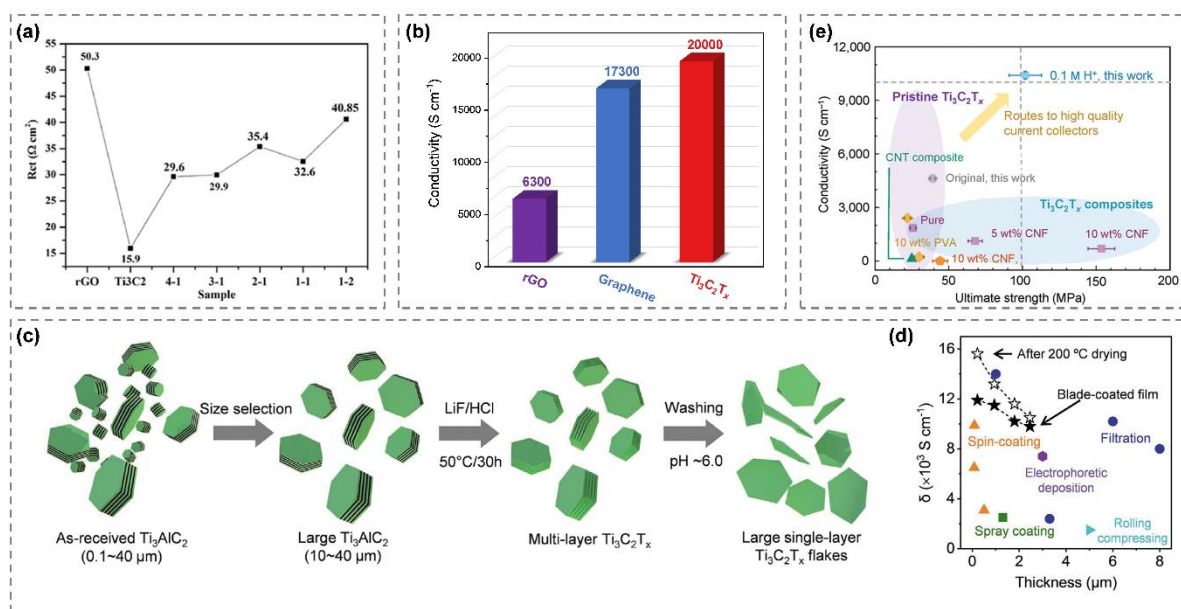
Figure 3. (a) Electron transfer resistance (R_{ct}) of $Ti_3C_2T_x$, rGO and other composited electrodes. Reproduced with permission.[83] Copyright 2018, American Chemical Society. (b) The electrical conductivity comparison between $Ti_3C_2T_x$,[32] graphene,[85] and rGO films.[84] (c) The synthesis process of large $Ti_3C_2T_x$ flakes from large Ti_3AlC_2 particles. (d) Electrical conductivity of blade-coated large $Ti_3C_2T_x$ films with increasing thickness before and after drying at 200 °C for 6 h. And those of other reported $Ti_3C_2T_x$ films made of different ways is presented here for reference. Reproduced with permission.[69] Copyright 2020, Wiley. (e)

10

Comparison of the strength and electrical conductivity of reported $Ti_3C_2T_x$-based film materials (typically the content of $Ti_3C_2T_x$ > 90 wt%). Reproduced with permission.[70] Copyright 2020, Wiley.

The surface groups of $Ti_3C_2T_x$ generated during the synthetic process have a significant impact on the conductivity, so as to the intercalants within $Ti_3C_2T_x$ layers. Computational results revealed a critical dependence of the electrical conductivity of $Ti_3C_2T_x$ on the surface property. For example, theoretical studies have shown that bare Ti_3C_2 monolayer is metallic with substantial electron states crossing the Fermi level. However, when –(OH) and –F surface groups are introduced into the structure by the etching process, $Ti_3C_2T_x$ turns to narrow bandgap metals or semi-conductors.[82, 89, 90] The factors determining metallic or possible semi-conducting behavior relates to the species and amount of surface groups as well as their corresponding arrangement.[82, 89, 90] Consequently, post-treatments on $Ti_3C_2T_x$ can also improve the electrical conductivity signficantly. For example, an increase in electrical conductivity of MXene films can be seen in a lower-temperature thermal treatment of $Ti_3C_2T_x$ films, as annealing at 200 °C has shown evidence to be effective to remove structural water molecules between $Ti_3C_2T_x$ layers due to synthesis, which resulted in the reduced resistance of $Ti_3C_2T_x$ films by 18% due to improved interlayer contact.[65] Further annealing $Ti_3C_2T_x$ films up to 775 °C resulted in the loss of intercalated water and surface groups (–(OH), –F) on $Ti_3C_2T_x$, which illustrated a decrease of resistance up to four times.[65] As for non-water based intercalants, Chen *et al.* recently utilized the proton acid of typical H^+ for the desorption of Li^+ (intercalants introduced in the synthesis method for $Ti_3C_2T_x$) from the nanosheet surface.[70] The H^+-exchanged $Ti_3C_2T_x$ films displays excellent conductivity (up to 10,400 S cm^{-1}), while the conductivity of $Ti_3C_2T_x$ films without H^+-exchange process is less than half (4,620 S cm^{-1}, Figure 3e).

2.2. Mechanical properties

2.2.1. High Strength

It has been proved that compared to other 2D nanomaterials like graphene, $Ti_3C_2T_x$-based films possess several advantages in mechanical properties. For example, a hollow cylinder made of 5-μm-thick $Ti_3C_2T_x$ can support about 4,000 times its own weight.[33] Generally, no primary bonding is introduced between the $Ti_3C_2T_x$ flakes in most film forming process, which indicates that inter-layer sliding is the main deformation mechanism during tensile loading in film (**Figure 4**a).[91] Based on the deformation mechanism, several influencing factors of mechanical properties of $Ti_3C_2T_x$ film can be explained easily. It has been reported that films made from large $Ti_3C_2T_x$ flakes have higher breaking strain, which can be ascribed to the long distances for larger flakes to slide before separation and/or fracture.[69] Moreover, binding between $Ti_3C_2T_x$ fakes may also render resistance in the form of mechanical interlocking when they are under stress. For example, density functional theory (DFT) studies identified that surface terminations (=O, –F, –(OH)) provide binding between flakes in the structure to withstand sliding forces.[92] In addition, positive ions introduced into the interlayers of $Ti_3C_2T_x$ flakes can strengthen $Ti_3C_2T_x$ film by the formation of ionic bonding located on the edges and the planes of $Ti_3C_2T_x$. The existence of ionic bonding multiplies the required energies to initiate the relative sliding of $Ti_3C_2T_x$ flakes. The introduction of K^+,[71] and Al^{3+},[72] have been proved successful to effectively enhance the mechanical properties of $Ti_3C_2T_x$ film.

Microscopic structural defects of $Ti_3C_2T_x$ film such as interlayered voids and wrinkles have a big impact on mechanical properties. The stress concentrations mainly focus on the vicinity of defects, which promote the generation of microcracks under increasing stress load. Once a critical crack has appeared, it will quickly spread along the whole cross section. Therefore, the reduction of the number of defect sites is vital to have an all-around improvement on the mechanical properties of $Ti_3C_2T_x$ film. For example, the current record for the tensile strength a $Ti_3C_2T_x$ film stands at 568 ± 24 MPa (Figure 4b). This tensile strength was achieved through the use of relatively larger $Ti_3C_2T_x$ flakes (10 ± 2 μm in lateral size) paired with a blade-coating technique.[69] Compared to vacuum filtration, the blade-coating technique can result in a highly

ordered MXene flakes, which deceases voids between the flakes, and leads to strong inter-flake interactions.

Flexible polymer materials can potentially improve the mechanical strength because polymers can create stronger bonds with MXene flakes. Synthetic polymers or natural macromolecules such as cellulose nanofiber[73], pyrrole,[93] and polyaniline[94] have been used as flexible additives or binders to enhance the mechanical performance of $Ti_3C_2T_x$ films. The improvement of mechanical properties is realized through the bond formation and synergistic effect between the inorganic MXene and organic polymer precursors.[2, 95] For example, Cao *et al.* reported a facile vacuum-assisted filtration self-assembly strategy to design the nacre-like microstructure of $Ti_3C_2T_x$ by mixing delaminated $Ti_3C_2T_x$ and cellulose nanofiber (CNF).[73] In this case, CNF promotes the generation of ordered lamellar structure of the composited films via intermolecular hydrogen bonding with the help of vacuum filtration. This bonding contributes greatly to the formation of the closely stacked layered structure so as to improve the toughness of $Ti_3C_2T_x$ films. This unique structure renders $Ti_3C_2T_x$/CNF composite films with high tensile strength (up to 135.4 MPa) and fracture strain (up to 16.7%) (Figure 4b), as well as excellent folding endurance (up to 14,260 times).[73] As demonstrated in Figure 4c, the fracture mechanism model can well explain the promising mechanical properties of the $Ti_3C_2T_x$/CNF films. When the stretching starts, the bonds between $Ti_3C_2T_x$ nanosheets and CNFs are broken and the $Ti_3C_2T_x$ sheets tend to slide over each other. Subsequently, the CNF molecular chains are stretched and prevent crack propagation before failure. After CNF failure, the composite film also displays signs of crack deflection, which can improve the mechanical properties. A more intuitive example, a hollow cylinder made of 5-μm-thick $Ti_3C_2T_x$ film can support about 4,000 times its own weight (Figure 4c).[33] By incorporating with 10 wt% polyvinyl alcohol (PVA), the film can be further strengthened to hold about 15,000 times its own weight without visible deformation or damage (Figure 4d).[33]

13

The mechanical strength of MXene films can also be improved by forming nanocomposites with other nanomaterials. For example, Zhou *et al.* fabricated the strong and super-tough $Ti_3C_2T_x$/rGO composited film first by a process that involved the reaction of exfoliated $Ti_3C_2T_x$ with exfoliated GO during filtration-based sheet fabrications.[74] As demonstrated in Figure 4e, the Ti–O–C covalent bond is formed at the $Ti_3C_2T_x$/rGO heterointerface via nucleophilic substitution and dehydration reaction, which is critical for assembling the hybrid architecture and reinforcing the linking of the $Ti_3C_2T_x$ between rGO nanosheets. As a consequence, after reduction by hydroiodic acid (HI), the tensile strength of the $Ti_3C_2T_x$/rGO (denoted as MrGO) sheet is 379.2 ± 2.5 MPa and the failure strain is $7.2 \pm 0.3\%$, which are 2.3 and 2.8 times higher than neat rGO sheet (a tensile strength of 165.8 ± 1.1 MPa and $2.6 \pm 0.3\%$).
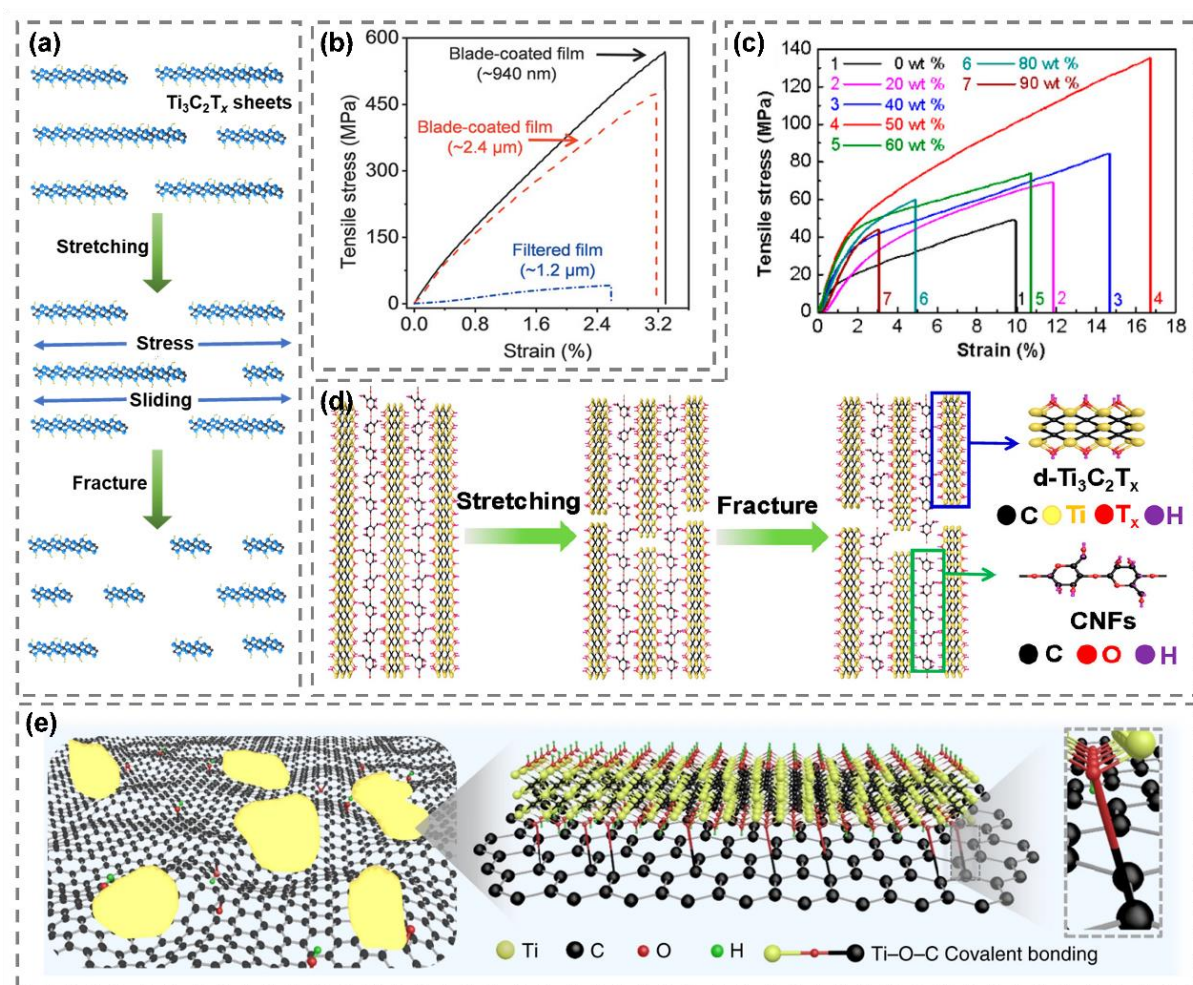

Figure 4. (a) Schematic illustration of the fracture mechanism of pure $Ti_3C_2T_x$ film. (b) Tensile stress–strain curves of $Ti_3C_2T_x$ film prepared by vacuum filtration and the blade-coating technique with large $Ti_3C_2T_x$ flakes.[69] (c) Tensile stress-strain curves of the $Ti_3C_2T_x$/CNF

14

composite film with different $Ti_3C_2T_x$ contents. (d) Schematic illustration of the fracture mechanism of the $Ti_3C_2T_x$/CNF composite film. Reproduced with permission.[73] Copyright 2018, American Chemical Society. (e) Schematic model of $Ti_3C_2T_x$/rGO platelets showing the formation of Ti–O–C covalent bonding. Reproduced with permission.[74] Copyright 2020, Nature Publishing Group.

2.2.2 Flexibility and foldability

Due to its excellent flexibility, $Ti_3C_2T_x$-based films can be easily deformed, which is a useful merit in the aforementioned applications. In order to intuitively understand the own flexibility of $Ti_3C_2T_x$, we only discuss the $Ti_3C_2T_x$ film without any additive in this part. For instance, freestanding $Ti_3C_2T_x$ films fabricated by filtration with proper mechanical property can be readily folded into various shapes, such as paper airplane (**Figure 5**a).[33] It is worth mentioning that a pure $Ti_3C_2T_x$ film with 3D macroporous architecture can still maintain the superior flexibility (Figure 5b), which indicates the strong moldability of $Ti_3C_2T_x$ films.[96] In addition, foldability is also one attracting property of $Ti_3C_2T_x$ films for flexible devices. As shown in Figure 5c, the $Ti_3C_2T_x$ film exhibits promising deformation stability in the process of bending and unbending at a certain humidity difference as the maximum bending angle is almost constant.[97] To further improve the foldability of $Ti_3C_2T_x$ film, Zhang *et al.* investigated the impact of the size of $Ti_3C_2T_x$ flakes and preparation methods on the foldability of $Ti_3C_2T_x$ film. They use a custom designed device as shown in Figure 5d to test the filtered and blade-coated $Ti_3C_2T_x$ films with two different flakes sizes under bending.[69] It is clear in Figure 5e that the blade-coated $Ti_3C_2T_x$ films with large $Ti_3C_2T_x$ flakes possess better deformation stability, which demonstrate negligible increase in resistance (about 0.4%) after bending at 180° for 5,000 cycles. In addition, the blade-coated $Ti_3C_2T_x$ film with large flakes has smooth edges, while there are obvious creases for filtered $Ti_3C_2T_x$ film with small flakes after bending at 180° (Figure 5f). It is concluded that the improved foldability could be ascribed to that the aligned flakes along the film plane improve the connectivity between flakes within the films and large flakes reduce the creases under bending. Additionally, evaluation of the electrochemical

performance of $Ti_3C_2T_x$ in flexible all-$Ti_3C_2T_x$ micro-supercapacitor toward flexible and wearable electronic was characterized under different bending angles during the device usage.[98] According to the cyclic voltammograms (CV) curves in Figure 5g, little change of the integrated area of the CV curves (< 20%) is observed during bending, which indicates the excellent foldability of the $Ti_3C_2T_x$ film. In addition to its application in energy storage and wearable electronics, $Ti_3C_2T_x$-based flexible films have been also widely studied in electromagnetic interference shielding, molecular sieving membranes, and pressure sensor applications, where the flexibility and foldability is usually necessary and will be introduced in the following section.
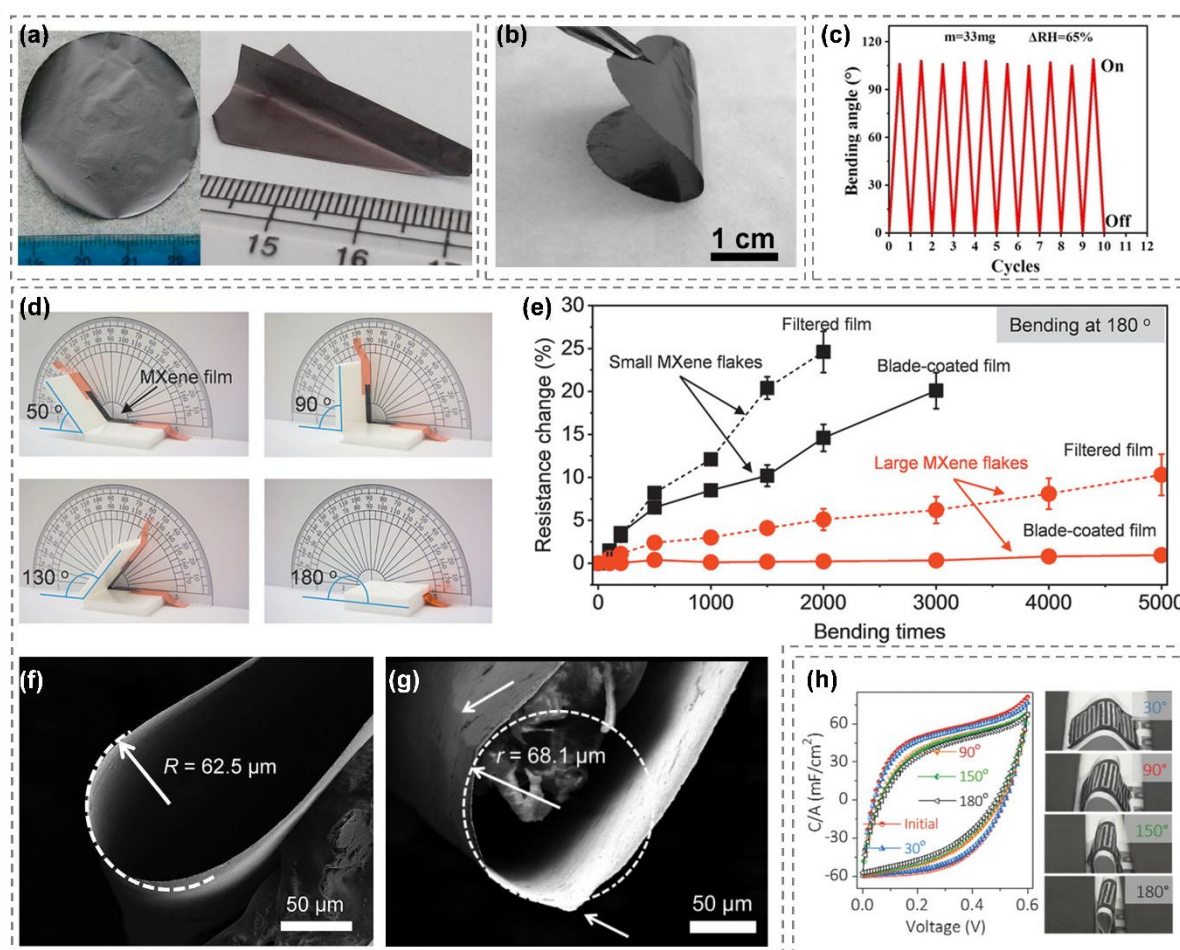
Figure 5. Mechanical flexibility. (a) The digtal photo of $Ti_3C_2T_x$ film and a $Ti_3C_2T_x$ film folded into the shape of a paper airplane. Reproduced with permission.[33] Copyright 2014, National Academy of Sciences. (b) Digital photos showing the flexibility of 3D macroporous $Ti_3C_2T_x$ film. Reproduced with permission.[96] Copyright 2017, Wiley. (c) Reversible and repeated bending of the $Ti_3C_2T_x$ film with the relative humidity difference of 65 %. Reproduced with permission.[97] Copyright 2017, Wiley. (d) Digital photos of a piece of $Ti_3C_2T_x$ film (1 cm × 4

16

cm) with a bend test. (e) Changes in resistance of different kinds of $Ti_3C_2T_x$ film after fully folded (180°). Scanning electron microscopy (SEM) images of (f) the blade-coated film with large flakes and (g) the filtered film folded at 180°. The creases are shown by arrows.[69] (h) CV curves of all-$Ti_3C_2T_x$ electrode under different bended states. Reproduced with permission.[98] Copyright 2018, Wiley.

2.3. Enhanced oxidation-resistance and shelf life of MXene films at different conditions

Experimental results showed that the oxidation of $Ti_3C_2T_x$ flakes is detrimental to the electrical conductivity and the electrochemical behavior of $Ti_3C_2T_x$.[75, 99] Previous investigations have identified that $Ti_3C_2T_x$ flakes are relatively stable in oxygen-free solvents or in dry air, but can be easily oxidized during reactions with oxygen and water, especially when exposed to light.[100] Once formed into films, the environmental stability of $Ti_3C_2T_x$ flakes is greatly improved compared to other forms of MXenes, such as dispersed flakes in water or powder.[77] Generally, oxidation of $Ti_3C_2T_x$ starts at the edges of flakes or at surface transition metal layer vacancy sites due to the exposure of thermodynamically metastable marginal Ti atoms, which leads to the formation of transition metal oxide nanocrystals (TiO_2).[32, 63, 101] Therefore, larger MXene flakes with a lower concentration of defects could slow the degradation of MXene monolayers due to oxidation. In MXene films, the $Ti_3C_2T_x$ surface is more directly exposed to air, which results in their oxidation, therefore thicker films with several $Ti_3C_2T_x$ 2D layers can form protective shells for the interior $Ti_3C_2T_x$ flakes. This means that it takes more time to fully degrade all the flakes, which makes $Ti_3C_2T_x$ films stable in ambient air within more than two months.[68] Notably, the storage condition plays an important role in the oxidation of $Ti_3C_2T_x$ film. As shown in **Figure 6**a, the electrical conductivity of $Ti_3C_2T_x$ film exposed to air drops quickly in the first few days. In other words, there are more reactive sites in the early stages of the experiment so that the oxidation goes faster. As the reactive sites reduce with time, the oxidation becomes slower.[99] Frozen $Ti_3C_2T_x$ has better oxidation prevention performance, which maintains the electrical conductivity well (Figure 6b). The slower oxidation can be ascribed to the slower kinetics due to the lower temperature. It is

worth noting that the humidity has a big impact on the oxidation and thus conductivity of $Ti_3C_2T_x$ films. Habib *et al.* found that $Ti_3C_2T_x$ films retained their conductivity well after 3 weeks while $Ti_3C_2T_x$ films stored in humid conditions experienced a decline in conductivity in an order of magnitude within 3 days.[99] As demonstrated in Figure 6c, both the tensile strength and fracture strain have different degrees of decline depending on the annealing time and temperature, which indicates that the oxidation also has an adverse effect on the mechanical properties of $Ti_3C_2T_x$ films.[102]

Recently, it has been proved that the introduction of intercalants such as Li^+[88] and $DMSO$[103] in the exfoliation step is the reason for the poor hydration stability.[70] Chen *et al.* reported that the absence of intercalated Li^+ in pure delaminated $Ti_3C_2T_x$ films blocks the intercalation of H_2O and further slows the diffusion of O_2 due to the densified structure and strong interaction between layers.[70] The Li^+-free $Ti_3C_2T_x$ films have better hydration stability than the original ones, which have no changes even in deionized water over a period of 100 days, providing a good solution to the oxidation challenge of $Ti_3C_2T_x$ films.[70]

The addition of flexible hydrophobic polymers is a potential approach to address the challenge of $Ti_3C_2T_x$ oxidation due to the polymer encapsulation of $Ti_3C_2T_x$ flakes, which can remarkably reduce the permeation of water and air. The incorporation of $Ti_3C_2T_x$ into hydrophobic polymers illustrates outstanding long-term stability without performance loss when exposed to air even after 20 weeks.[3] These features lend properties which greatly contribute to practical applications of $Ti_3C_2T_x$-based films, such as water purification, where the exposure to air or wet conditions is inevitable.[77]

While MXene flakes have high mechanical strengths, their thin freestanding films can have lower mechanical properties and can be torn manually or get damaged during storage in a humid environment. This is ascribed to interlayer bonds between the MXene flakes that are significantly weaker than the primary intralayer bonds and water molecule would intercalate in MXene films.[70, 91] Additionally, since MXene films can be used as water membranes (more

details can be found in Section 3.4), the stability of MXene films in water is important. Introduction of flexible polymer materials is a potential approach to improve the shelf life because polymers can create stronger bonds with MXene flakes and encapsulate them, which remarkably reduces the permeation of water and air. For example, $Ti_3C_2T_x$/natural rubber (NR) composite films were prepared by Yang *et al.* using a vacuum filtration of the mixed suspension containing $Ti_3C_2T_x$ and NR.[75] The strong interaction between NR and $Ti_3C_2T_x$ results in the formation of lightweight, interconnected, and hydrophobic composite films. After the soaking in water for 5 days, cracks appear in the pure $Ti_3C_2T_x$ films, while both $Ti_3C_2T_x$/NR20% and $Ti_3C_2T_x$/NR60% films maintain their original morphology. When treated under water for 15 days, bare $Ti_3C_2T_x$ films broke into several fragments while no crack was noted in the $Ti_3C_2T_x$/NR60% film, indicating that $Ti_3C_2T_x$/NR60% film retained its original shape with no obvious damage, showing excellent durability (Figure 6d). It can be expected that, with the enhanced durability in both water and air environment, $Ti_3C_2T_x$-based films can gradually move from the laboratory to the commercialization of related devices.[104]

Although obvious enhancement in shelf life of MXene-based films has been achieved by the introduction of polymer, most conventional polymers are limited by their low glass transition temperature and low temperature stability (below 200 °C). For instance, CNF can provide intermolecular hydrogen bonding for MXene flakes to improve the tensile strength of MXene-based film.[73] However, due to the lack of strong and symmetric aromatic rings within backbone, CNF is sensitive to temperature since it has a low decomposition temperature of about 230 °C, which prevents MXene-CNF film uses in high temperature environments.[105] In order to achieve superior durability of MXene-based film at higher temperatures, rational polymer selection must be considered. Lei *et al.* chose the rod-like instead of worm-like aramid nanofiber (ANF) to mix with $Ti_3C_2T_x$ by self-assembly in solution to produce highly robust and temperature-stable $Ti_3C_2T_x$/ANF films.[76] The rod-like ANF has good interfacial adhesion with $Ti_3C_2T_x$ flakes because of the strong hydrogen-bond interactions between layers, which results

in the excellent durability of the composite film. Even folded for 10,000 times, the $Ti_3C_2T_x$/ANF film preserved the original mechanical properties. More important, the $Ti_3C_2T_x$/ANF film owns a broad range of working temperatures from -100 °C to 300 °C with an acceptable tensile strength variation (335 to 136 MPa). As employed in electromagnetic interference (EMI) shielding, the value of EMI shielding remains stable from 23.6 to 26.3 dB with a big temperature variation from -100 °C to 300 °C (Figure 6e). The superior temperature stability is attributed to the strong and symmetric aromatic rings in the backbone unit of ANF and strong interactions between ANF and $Ti_3C_2T_x$, which makes the $Ti_3C_2T_x$/ANF film's decomposition temperature as high as 400 °C. Figure 6f intuitively demonstrates the stability, where the $Ti_3C_2T_x$/ANF film cannot be ignited for a period of time on a burning alcohol lamp due to the inherent components of films.


20
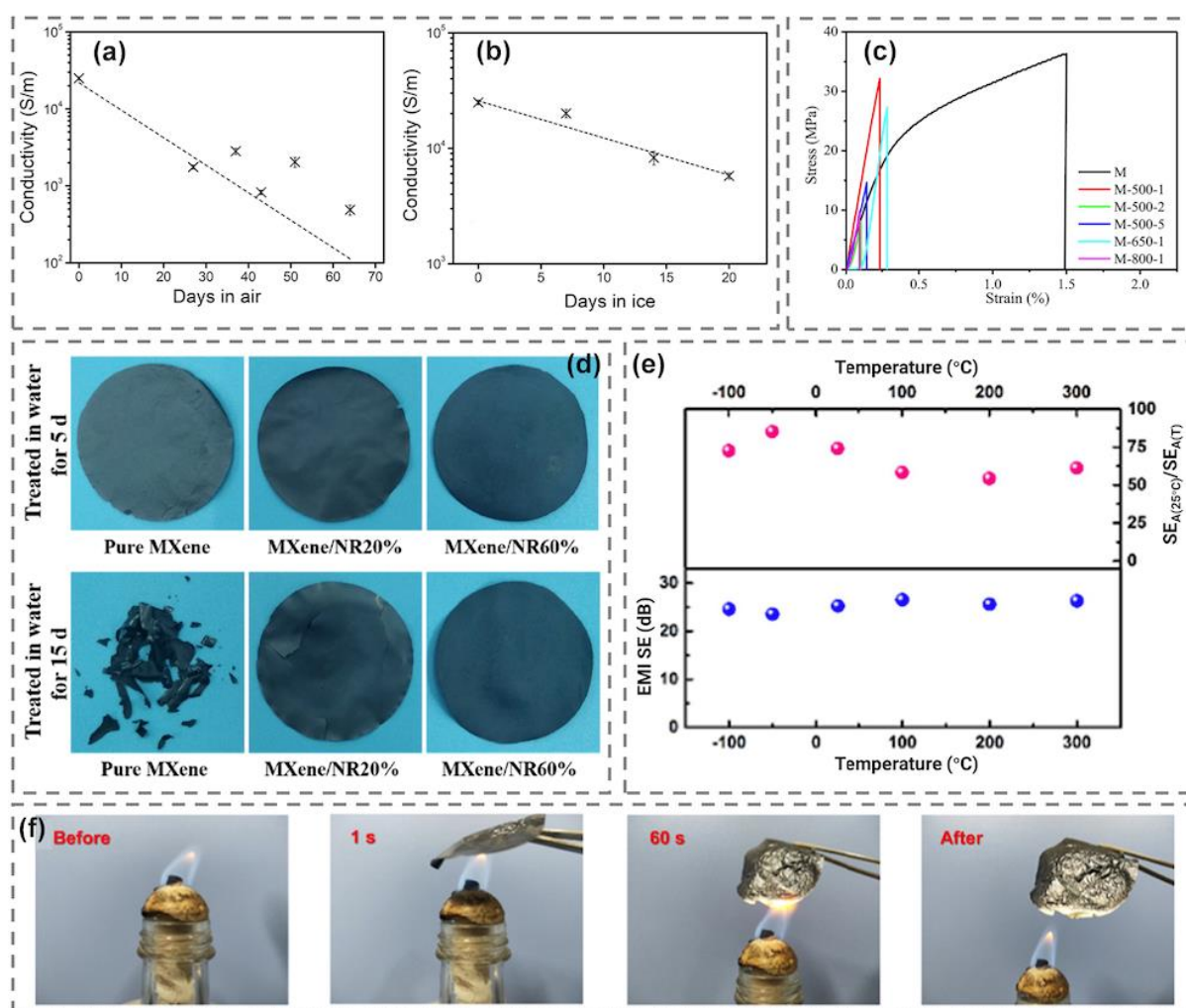
Figure 6. Variation of electrical conductivity with time for (a) $Ti_3C_2T_x$ films in air and (b) films made from aged $Ti_3C_2T_x$ dispersed in ice. Reproduced with permission.[99] Copyright 2019, Nature Publishing Group. (c) Stress-strain curves of various $Ti_3C_2T_x$ films (M presents $Ti_3C_2T_x$ film and the numbers present annealing temperature and time). Reproduced with permission.[102] Copyright 2020, Elsevier. (d) Digital photos of pure $Ti_3C_2T_x$ and $Ti_3C_2T_x$/NR composite films after the treatment under water for 5 d and 15 d. Reproduced with permission.[75] Copyright 2020, Elsevier. (e) The variation of EMI shielding performances and SE_A/SE_T values of MXene/ANF film under different temperatures. (f) Digital images of $Ti_3C_2T_x$/ANF film before and after burning. Reproduced with permission.[76] Copyright 2020, American Chemical Society.

2.4. Hydrophilicity/hydrophobicity

As discussed, due to their wet etching process, $Ti_3C_2T_x$ nanosheets are terminated by function groups such as –O and –(OH). As a result, $Ti_3C_2T_x$ nanosheets are negatively charged, and have an excellent hydrophilic surface. Due to the hydrophilicity and electrostatic repulsion between neighboring nanosheets, $Ti_3C_2T_x$ aqueous suspension quite stable, and it also exhibits a prominent Tyndall effect (**Figure 7**a).[80] It is noteworthy that this hydrophilicity and water stability imply that the processing can be achieved in aqueous phase. Hence, $Ti_3C_2T_x$ nanosheets are able to be processed via solution-based methods.[106-109] It also bodes well for the use of $Ti_3C_2T_x$ in applications where water is involved, such as membrane separation and desalination.[110] Compared to the high-concentration HF etching methods, less harsh etching processes (like the LiF/HCl method) can increase –OH and –O groups on $Ti_3C_2T_x$, which leads to improved hydrophilicity. Surface hydroxylation is considered to be the most common and simple strategy to further improve the ability of hydrophilicity of $Ti_3C_2T_x$. The terminal group of Ti–O_x on $Ti_3C_2T_x$ surface can be transformed to Ti–$(OH)_x$ by HCl treatment without other complex manipulations, which improves the wettability of $Ti_3C_2T_x$-based films, and contributes to unlock the potential of related fields, such as water purification.[77, 111]

Notably, the hydrophilic nature of pure $Ti_3C_2T_x$ or the inorganic hybrids leads to the adsorption of humidity and gases from the environment, which affects the stability and reliability of $Ti_3C_2T_x$ for some applications such as pressure sensing under ambient conditions. Another major challenge for the applications of $Ti_3C_2T_x$-based films is the swelling behavior

due to the poor hydration stability,[112] which directly correlates to a durability issue due to the deterioration in both mechanical and electrical properties.[78, 113] Therefore, there is a need to fabricate a hydrophobic $Ti_3C_2T_x$-based film for having a better performance in some applications where waterproof is in need. Gogotsi *et al.* developed a convenient strategy that incorporated multi-layer $Ti_3C_2T_x$ particles into the hydrophobic polymer polyvinylidene fluoride trifluoroethylene (P(VDF-TrFE)) and prepared hydrophobic, flexible, and freestanding films via spin-coating.[3] The $Ti_3C_2T_x$/P(VDF-TrFE) films display a higher contact angle of 90°, demonstrating the hydrophobicity of the surface of the hybrid film (Figure 7b). The hydrophobic P(VDF-TrFE) shell on the outside of $Ti_3C_2T_x$ particles is beneficial for the stability of $Ti_3C_2T_x$ by protecting the entirety from oxidation. Different from conventional polymer doping, Liu *et al.* first used hydrazine-induced foaming process to obtain hydrophobic and porous $Ti_3C_2T_x$ films with excellent water resistance (denoted as MXene foam).[78] The hydrophobic mechanism, as revealed in Fig. 7c, is also of great reference significance. The Ti–OH groups on the surface of $Ti_3C_2T_x$ react with hydrazine to generate water vapor by the chemical reaction of $OH + OH \rightarrow H_2O + O$,[114, 115] while the C–(OH) groups attached to the carbon layers convert into CO or CO_2 reduced by hydrazine.[116] These reactions eliminate the hydrophilic terminations such as the hydroxide groups, successfully indicating the transform from hydrophilicity to hydrophobicity, which is confirmed by the water contact angle measurements and long-term stability test of the MXene foam (Figure 7d–f).
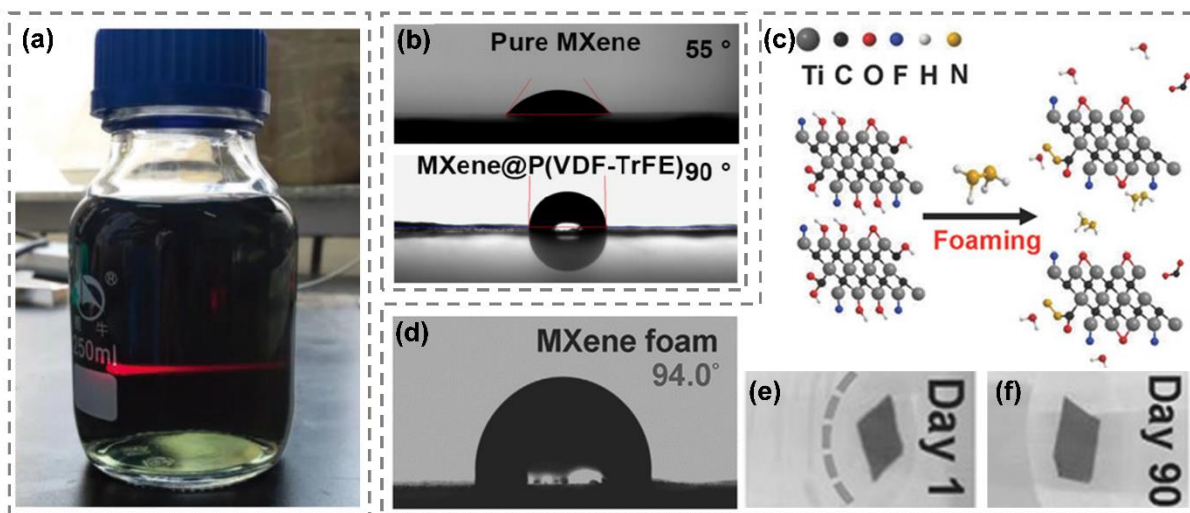
Figure 7. (a) Digital photo of the diluted $Ti_3C_2T_x$ colloidal solution, exhibiting a green color and clear Tyndall scattering effect. Reproduced with permission.[80] Copyright 2018, Wiley. (b) Water contact angle measurements of a pure $Ti_3C_2T_x$ film and a $Ti_3C_2T_x$/P(VDF-TrFE) film. Reproduced with permission.[3] Copyright 2020, American Chemical Society. (c) Foaming mechanism of the hydrophobic $Ti_3C_2T_x$ film. (d) Water contact angle measurements of the MXene foam. Water tolerance of the MXene foam from (e) 1 day to (f) 90 days. Reproduced with permission.[78] Copyright 2017, Wiley.

2.5. Porosity: sub-nano to micron size pores

As compared to the 2D nanosheets with smooth and flat surfaces, porous $Ti_3C_2T_x$-based films offer advantages for the enhancement of the film performance for target applications, especially for electrochemical energy storage. The porous nanostructures provide large effective surface areas and abundant active sites for electrochemical reactions, which significantly contributes to the improvement of specific energy density. Additionally, the porosity of $Ti_3C_2T_x$-based films can ensure the effective wetting and penetration of electrolyte to the electrode surface. In recent years, porous $Ti_3C_2T_x$-based films with desirable architectures have been constructed by different synthetic strategies. The methods of making pores in $Ti_3C_2T_x$-based films can be divided into three categories. The first method is the hard-templating strategy, which is convenient and effective to fabricate porous films. For example, it is relatively easy to obtain porous $Ti_3C_2T_x$-based films by freeze-drying using ice as the hard template.[79] Meanwhile, the pore size of $Ti_3C_2T_x$-based films can also be tuned. For instance, Zhao *et al.* adopted a simple

sulfur-template method to acquire a developed porous architecture (**Figure 8**a).[54] With the increase of sulfur content, the porous $Ti_3C_2T_x$ films (denoted as p-MXene-35, 48 and 71 based on the sulfur content) had more pores and larger pore sizes, as shown in Figure 8b.

Porous $Ti_3C_2T_x$-based films can also be obtained through the introduction of functional materials such as CNTs[117] and rGO[83] to construct more open structures. The existence of porous structure is in favor of withstanding the self-restacking tendency. Furthermore, the introduced materials may increase the conductivity of whole films or strength the $Ti_3C_2T_x$-based films due to increased durability in hostile environments, such as corrosive, oxidative, high strain conditions. Fan *et al.* have used porous graphene as substrate to prepare freestanding $Ti_3C_2T_x$/holey graphene film by filtration of the alkalized $Ti_3C_2T_x$ and porous graphene oxide dispersions.[80] The $Ti_3C_2T_x$/holey graphene hybrid films immensely shorten the transport path and accelerate both ion and electron transportation rates. Ren *et al.* adopted chemical-etching method using Cu^{2+} cations as the catalyst to partially oxidize $Ti_3C_2T_x$ nanosheets in the water.[81] When this partial oxidation is followed by acid treatment to remove the metal oxide, mesoporous $Ti_3C_2T_x$ (denoted as p-$Ti_3C_2T_x$) flakes can be obtained (Figure 8c). Figure 8d and e illustrate a schematic of the resulting in-plane pores and their sizes that are about tens of nanometers. The p-$Ti_3C_2T_x$ assembled film electrodes with porous structure demonstrated a five-fold increase of capacity compared to the non-porous structure. Further research efforts should be focus on addressing the challenges originating from the porous structures. For example, porous $Ti_3C_2T_x$-based films are more vulnerable to oxidation when exposed to the air compared to the compact counterpart.[63] Moreover, the decrease of density due to the porous structure would result in relatively low volumetric capacities when applied in energy storage devices.
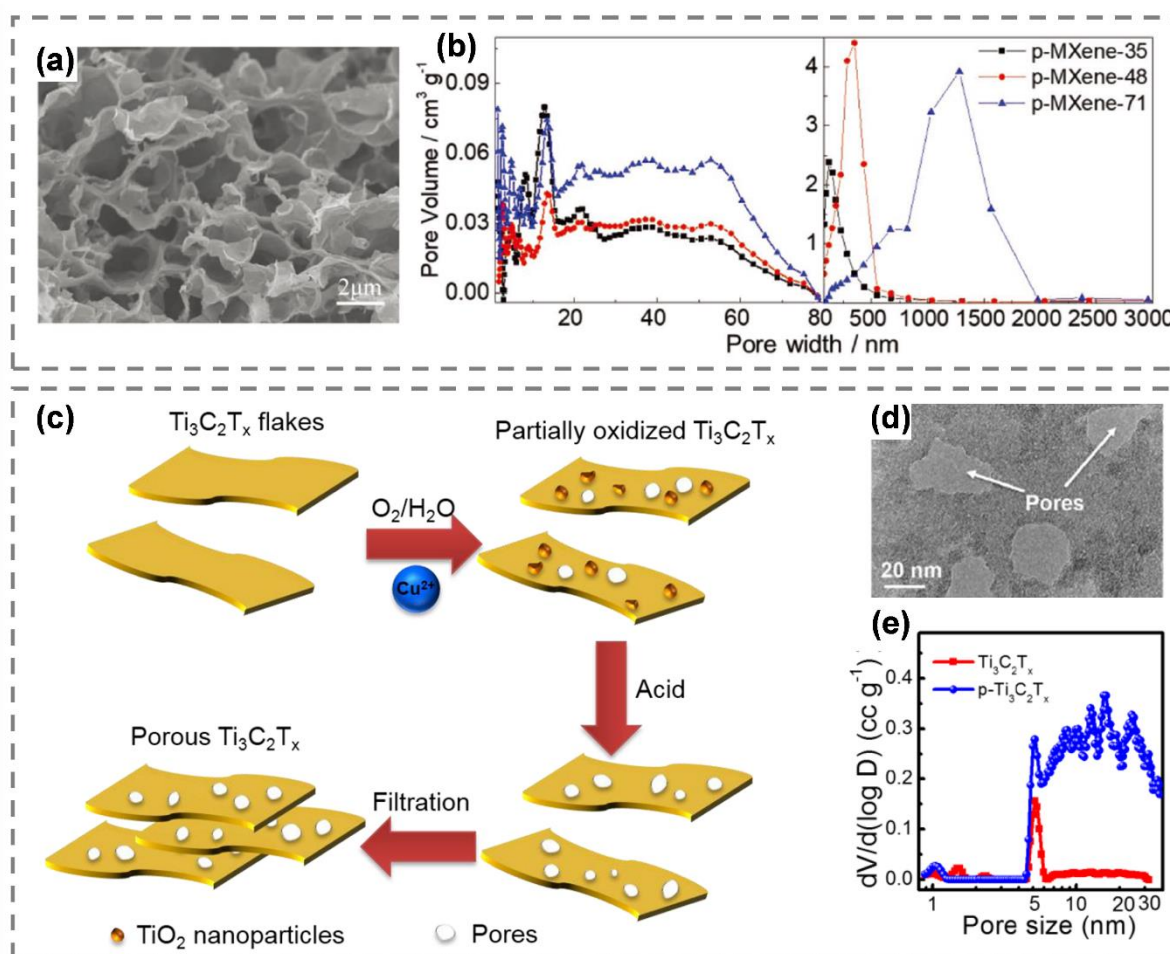
Figure 8. (a) SEM images of the porous $Ti_3C_2T_x$. (b) Pore size distribution from the nitrogen sorption and mercury intrusion porosimetry results. Reproduced with permission.[54] Copyright 2019, Wiley. (c) Schematics showing the chemical etching of $Ti_3C_2T_x$ flakes to form porous structure. (d) Transmission electron microscopy (TEM) image of $Ti_3C_2T_x$ flakes after chemical etching in 0.2 M $CuSO_4$ solution at room temperature. (e) Pore size distribution of different samples. Reproduced with permission.[81] Copyright 2016, Wiley.

2.5.1. Ions/molecules sieving effect

Due to few-atom thicknesses of 2D materials, they are able to minimize the transport resistance of membranes to realize high-throughput separation. Moreover, the sub-nanometer interlayer spacing allows highly selective mass transport through the resulting membranes. For example, MoS_2 and graphene oxide (GO) membranes have been reported to sieve inorganic salts or organic molecules with high water permeability.[118, 119] However, they are difficult to be used for precise separation of small molecules with size down to sub-nanometer. In this realm, interest in $Ti_3C_2T_x$ as a potential candidate for developing 2D-material separation

membranes has grown, which exhibited excellent performances for water purification or molecular sieving beyond the limits for state-of-the-art membranes.[77]

MXene films have shown promise as gas membrane as well. **Figure 9**a shows H_2-selective $Ti_3C_2T_x$ sheets channels and it is proved that $Ti_3C_2T_x$-based film has a high separation factor of H_2/CO_2. CO_2 has a much larger quadrupole moment, which has a strong interaction with the $Ti_3C_2T_x$ film. The adsorbed CO_2 molecules in the sub-nanochannels can even block the passing molecules, resulting in the increasing resistance to CO_2 diffusion, while such phenomenon is absent for H_2.[120] In addition, it is found that gas permeance decreased while the selectivity increased with $Ti_3C_2T_x$ layer thickness (Figure 9b).[113] Notably, water molecules intercalated between the $Ti_3C_2T_x$ layers also affect the gas transport behaviors. When the relative humidity (RH) increased from 10% to 40%, the mixed H_2/CO_2 selectivity remains almost unchanged. However, under high relative humidity (RH = 90%), the $Ti_3C_2T_x$ films shows a 40% decrease of H_2 permeance, and the mixed H_2/CO_2 selectivity also reduces from 19.7 to 9.8 compared with the $Ti_3C_2T_x$ films tested in 40% RH because the presence of large amount of water between the $Ti_3C_2T_x$ layers can significantly hinder the transport of H_2 molecules.[113] Figure 9c shows that the 20-nm-thick $Ti_3C_2T_x$ film, which exhibits excellent molecular separation properties for H_2/CO_2 gas pair: permeance of H_2 is up to 1584 GPU and H_2/CO_2 selectivity reaches to 27. This separation efficiency exceeds above the 2008 Robeson upper-bound for polymeric membranes.[121] Similarly, the selectivity for H_2/C_3H_8 gas pair reaches as high as 110, indicating that pristine $Ti_3C_2T_x$ nanofilm has extraordinary molecular sieving capability with molecular differentiation size down to sub-nanoscale dimensions.

In addition, $Ti_3C_2T_x$ films also illustrate an attractive performance for the charge and size selective rejection of ions and molecules. Due to the hydrophilic nature of $Ti_3C_2T_x$ and the presence of structural water between the layers, $Ti_3C_2T_x$ films possess ultrafast water flux. Compared to GO, single-charged cations showed comparable permeation rates for both $Ti_3C_2T_x$ and GO, but $Ti_3C_2T_x$ films demonstrate significantly lower permeation rates for multiple-

charged ions (Figure 9d and e).[122] In other word, GO is unable to separate ions with different charges, while $Ti_3C_2T_x$ films demonstrate a better performance in the separation of higher charge cations.
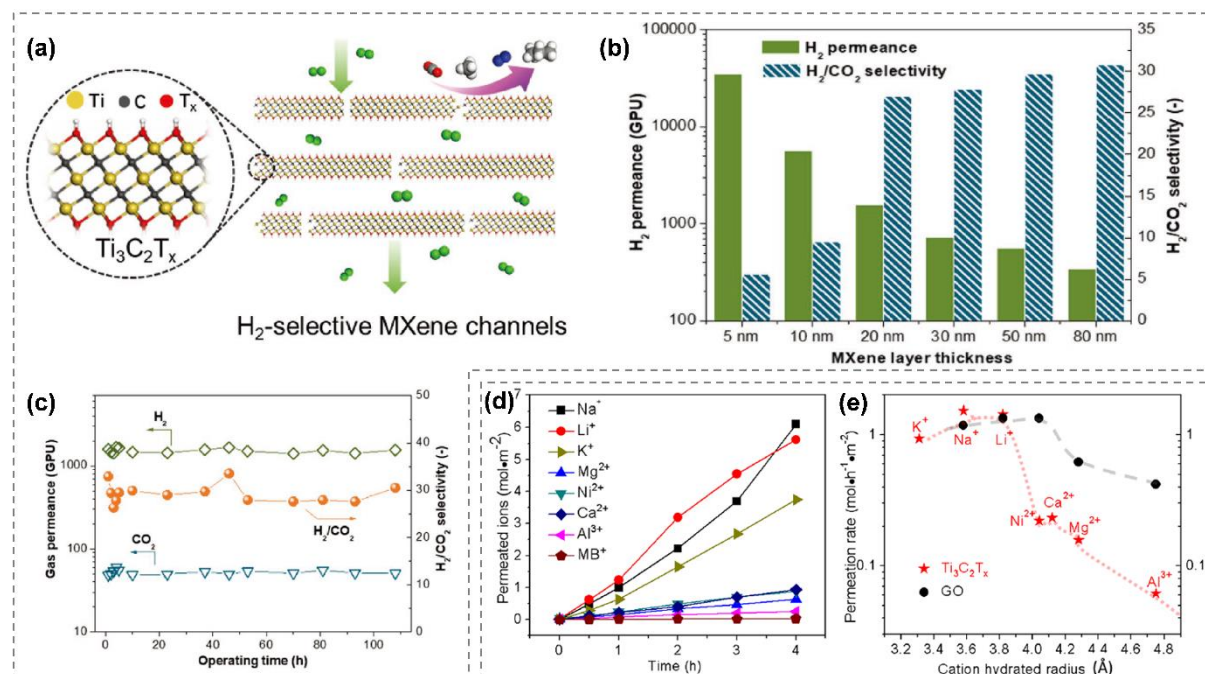
Figure 9. $Ti_3C_2T_x$ ions/molecules sieving. (a) Structures and gas transport of H_2-selective $Ti_3C_2T_x$ nanofilms. (b) Influence of $Ti_3C_2T_x$ nanofilm thickness on the H_2/CO_2 separation performance. (c) H_2/CO_2 long-term operation test. Reproduced with permission.[113] Copyright 2018, Wiley. (d) Number of cations permeated through the $Ti_3C_2T_x$ films against time. (e) The permeation rates of cations against their hydration radii through the $Ti_3C_2T_x$ and GO films. Reproduced with permission.[122] Copyright 2015, American Chemical Society.

2.6. The Convenient processability

The good dispersibility of $Ti_3C_2T_x$ flakes in a large range of possible solutions simplifies the film-forming process. Unlike complex film forming techniques such as chemical vapor deposition, MXenes' solution processability enables methods such as spray-coating,[68] electrophoretic deposition,[123] or vacuum filtration.[124] The presence of abundant surface functionalities on MXenes is the basis of the convenient solution processability. This makes MXenes superior to other materials which require additives such as binders and surfactants for the fabrication of films, which can competitively benefit the purity and the electronic properties of MXene films in comparison .[125] The stability of MXene in the solution is determined by the

surface functionalities through the interactions between MXene and solvent, which can be affected by the composition of MXenes' surface groups. [126] The tunable potential of MXenes' surface groups makes MXene competitive for various film forming techniques. MXene solutions or inks are viscoelastic materials, which indicates their rheological behavior contain both viscous and elastic characteristics. The flow behavior is determined in large part by the concentration of MXene and the aspect ratio of its flakes. For example, compared to multilayer counterparts and other nanomaterials, the dispersions demonstrate a sharp viscosity rise by increasing their concentration due to the high aspect ratio of the flakes.[127] Based on the difference between monolayer and multilayer MXene in rheological behavior, it is necessary to have a reasonable choice of the type of MXene solution for specific application. For example, if there is a strong demand of deposition of a thick film, the extremely high viscosity of the high concentration monolayer MXene solution will make them incompatible with most film forming techniques. Interestingly, even dilute dispersions of MXene (about 0.36 mg mL^{-1}) have a high level of elastic behavior, which could contribute to some film forming techniques such as spin-coating.[126, 128, 129] Besides, these solution-based processes result in freestanding Ti$_3$C$_2$T$_x$-based films, which have great application potential in many fields[48, 68, 96] including the energy storage and water purification. Specifically, the freestanding film can be directly used as an electrode without a metal current collector for high performance batteries or supercapacitors. Different from the conventional rigid electrodes, Ti$_3$C$_2$T$_x$ nanosheets not only provide good integrity and flexibility as the binder and flexible backbone but also establish a continuous conductive network for the fast transfer of electrons. In addition, the ease of assembly of Ti$_3$C$_2$T$_x$-based films into the energy storage device is beneficial to the future commercialization. Moreover, by avoiding any inactive components including polymer binder, conductive agent, and current collectors used in the conventional electrode fabrication, Ti$_3$C$_2$T$_x$-based films could result in excellent volumetric capacity, which is highly useful for wearable electronic devices. As for applications in the field of water purification, Ti$_3$C$_2$T$_x$-based films also feature convenient

processability because of the good mechanical properties. For example, it is time-saving and cost-effective to separate $Ti_3C_2T_x$-based films after water purification while the separation of the powder materials needs to adopt strategies such as flocculation and centrifugation.

3. Applications and performance optimization strategies of titanium carbide (MXene)-based films

MXene-based films have demonstrated competing performances in a broad range spectrum of applications, including lithium-/sodium-ion storage, (micro-)supercapacitors, transparent conductive electrodes, and water purification (**Figure 10**). Although tremendous advances have been achieved, there are still some challenges to be addressed to improve the performance of MXene-based films for practical applications and diverse optimization strategies have been developed to endow the resultant MXene-based films with enhanced performances. In this section, we will summarize the state-of-the-art progress on the approaches from the aspects of structure design, surface modification of MXene flakes, and optimization of film forming processes, to facilitate the application prospects of MXene-based films for target applications.
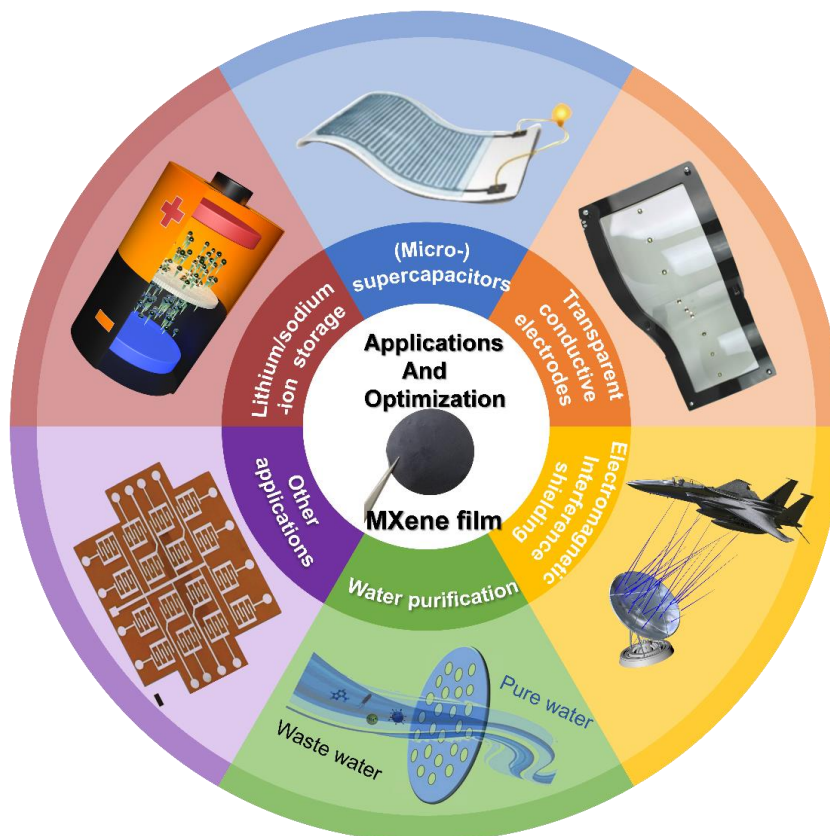
Figure 10. Applications of titanium carbide (MXene)-based films.

3.1. Lithium-/sodium-ion storage

2D materials are one of the great candidates for energy storage devices due to their association of high specific surface area, abundant active sites and continuous charge transport pathway.[49, 130-133] In recent years, MXenes have emerged as a rising star in the field of lithium-/sodium-ion storage. Compared to MXene powder, MXene-based films are more convenient for electrode applications without the need for extra steps and additive materials for the electrode fabrication process. However, the electrochemical performance of MXene-based films is compromised due to the restacking of MXene nanosheets, which hinders electrolyte infiltration and thus ion transportation. For example, pure $Ti_3C_2T_x$ film can provide capacities about 160 mAh g^{-1},[134] and 25 mAh g^{-1},[117] for lithium- and sodium-on storage, respectively.

To make better use of MXene-based films for energy storage, a series of strategies have been developed to prevent MXene nanosheets from restacking.[54] Introducing the interlayer spacers

into MXene-based films presents a direct and effective approach to prevent the restacking of MXene nanosheets and facilitate electrolyte transport and access of ions to the electrode. Thus far, interlayer spacers of surfactants,[135] carbon nanotubes (CNTs),[136] polymer[137], and rGO[138], have been reported. For example, by introducing the positively charged 1D CNTs as spacers, Xie et $al.$ fabricated porous $Ti_3C_2T_x$/CNT composite film electrodes via electrostatic self-assembly for sodium-ion storage (**Figure 11**a).[117] As revealed in Figure 11b, the self-stacking of 2D $Ti_3C_2T_x$ flakes were effectively separated via the electrostatic incorporation of CNTs and the $Ti_3C_2T_x$/CNT films achieved a high reversible capacity of 175 mA h g^{-1} for electrochemical sodium-ion storage at 0.02 A g^{-1}, which was about 4.6 times higher than that of the pure $Ti_3C_2T_x$ films electrode (Figure 11c).

The introduction of materials with high lithium-/sodium-ion storage capacity as the interlayer spacer was favorable for further improving the specific capacity of electrode at the system level. Recently, Tian et $al.$ covalently anchored silicon (Si) nanospheres on the highly conductive networks based on $Ti_3C_2T_x$ sheets (Figure 11d) by vacuum filtration.[139] This unique layered architecture of $Ti_3C_2T_x$ can accommodate the large volume expansion of silicon nanoparticles which enhances the conductivity of the composite and brings additional active sites. As a result of the introduction of silicon with high specific capacity and architecture optimization, the hybrid films showed superior electrochemical performance with high stable capacity of 2,118 mA h g^{-1} at 0.2 A g^{-1} after 100 cycles. Even at 5 A g^{-1}, the capacity retention of Si/$Ti_3C_2T_x$ was still maintained at 51.33% (Figure 11e).[139] In contrast, the pure Si anode exhibits a fast decay of capacity under the same conditions (Figure 11f). To our best knowledge, it is the highest value of reported freestanding electrodes for lithium-ion storage, showing a great potential for practical applications.

Another effective strategy to prevent the restacking of MXene nanosheets is to construct 3D porous architecture of MXene-based films. For example, Ma et $al.$ constructed a 3D porous structure of the $Ti_3C_2T_x$/rGO hybrid film by an electrolyte-induced self-assembly method.[83]

The addition of GO and NH_4HCO_3 as the electrolyte transformed the dense-stacked $Ti_3C_2T_x$ film to a 3D porous structure. In detail, the existence of NH_4^+ broke the electrostatic balance between MXene and GO flakes, leading to the formation of $Ti_3C_2T_x$-GO clusters. During the following dehydration process by vacuum filtration, the hybrid microclusters gradually cross-linked to form the 3D porous structure, which effectively facilitated the diffusion of electrolyte in the film electrode. When employed as an anode for lithium-ion storage, the $Ti_3C_2T_x$/rGO hybrid films deliver a high specific capacity of 335.5 mA h g^{-1} at 0.05 A g^{-1} with long-term cycling stability.[83] The rate performance and specific capacity of the hybrid film outperform that of both the pure $Ti_3C_2T_x$ and rGO films, which demonstrates the advantage of 3D porous architecture in improving the electrochemical property. Zhao *et al.* adopted a template method to process of 2D $Ti_3C_2T_x$ flakes into freestanding, flexible, and highly conductive 3D macroporous films (Figure 11g).[96] As revealed in Figure 11h, the 3D macroporous $Ti_3C_2T_x$ show good capacity retention with increasing current rates and achieve a reversible capacity of 330 mA h g^{-1} at 0.25 C, which is better than multilayer $Ti_3C_2T_x$ particles[140] and porous $Ti_3C_2T_x$/CNT hybrid films.[117]
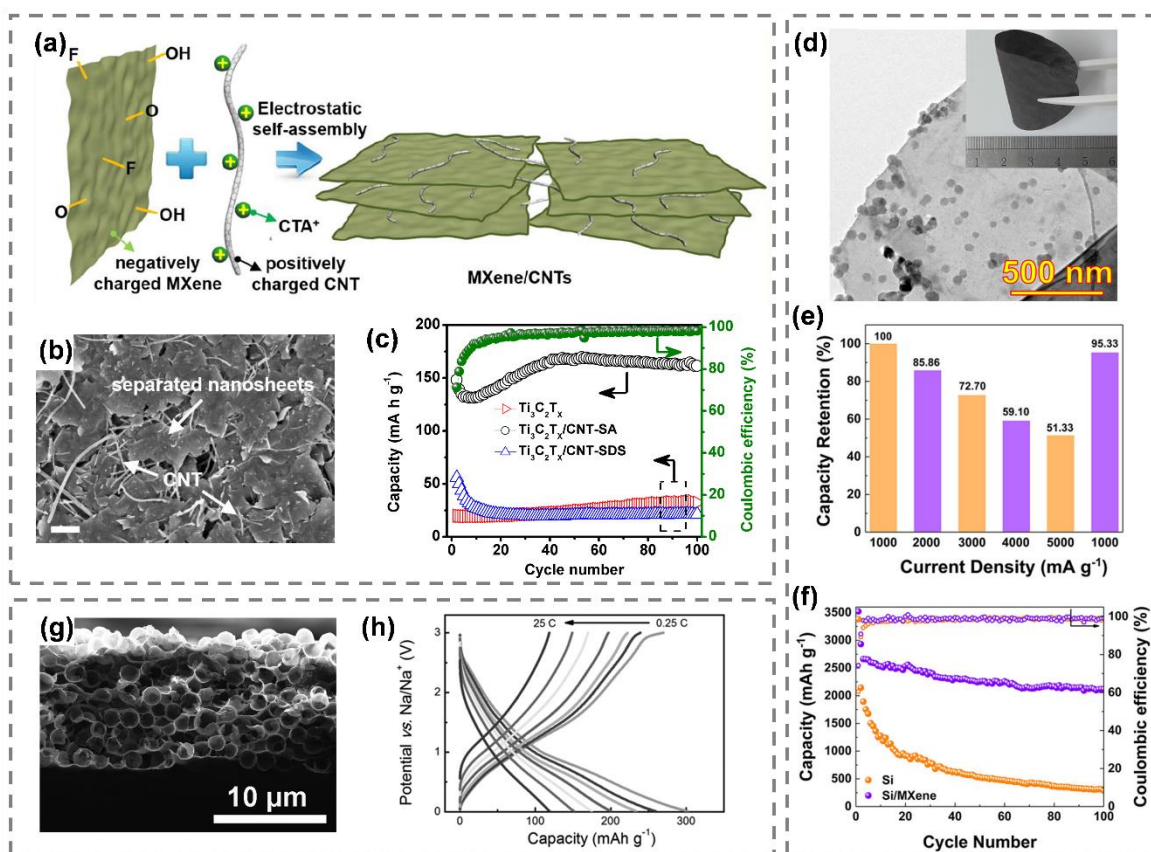
Figure 11. (a) Schematic showing preparation of the porous $Ti_3C_2T_x$/CNT electrode by the self-assembly method. (b) Top view SEM images of porous $Ti_3C_2T_x$/CNT films. (c) Cycling performance of different samples at a current density of 0.2 A g^{-1} from the second cycle. Reproduced with permission.[117] Copyright 2016, Elsevier. (d) TEM imagine of the $Si/Ti_3C_2T_x$ (inset shows the photograph of the flexible films). (e) Capacity retention of $Si/Ti_3C_2T_x$ anodes at varied current densities from 1 to 5 A g^{-1}. (f) Cycling stability of $Si/Ti_3C_2T_x$ and pure Si anodes at 0.2 A g^{-1}. Reproduced with permission.[139] Copyright 2019, American Chemical Society. (g) Cross-sectional SEM images of the 3D porous $Ti_3C_2T_x$ film. (h) Charge–discharge curves of 3D macroporous $Ti_3C_2T_x$ film electrodes at different current densities.[96]

3.2. (Micro-)supercapacitors

As shown in **Figure 12**a, MXenes feature fast electron supply to electrochemically active sites due to the conductive transition metal carbide layer, unique 2D layered structure and pre-intercalated water, all of which can contribute to the improvement of electrochemical performance.[66] It has been demonstrated that the pseudocapacitance of $Ti_3C_2T_x$ mainly comes from the redox reactions of Ti atoms.[141, 142] Furthermore, MXene-based freestanding films are appealing because of their ultrathin, lightweight, and flexible characteristics, which are the desirable features for flexible supercapacitors.

However, the application of MXenes-based films for supercapacitors encounters a similar challenge mentioned in lithium/sodium-ion storage, self-stacking of the 2D flakes, which prolongs the paths for ions. The electrochemical performance of MXenes-based films electrode of supercapacitors can be further improved by structure design and surface modification. The conversion of MXene films to a porous structure is a common but effective strategy to mitigate these issues.[80] Lukatskaya *et al.* have revealed the difference of layered stack structure (formed by vacuum filtration of the $Ti_3C_2T_x$ solution) and porous structure of $Ti_3C_2T_x$-based films (formed by using polymethyl methacrylate (PMMA) spheres as template to create open structure) as electrodes in supercapacitors (Figure 12b and c).[66] The compact structure of the filtered film (denoted as HG-Ti_3C_2) limited high-rate charge transfer and impeded ion transport towards redox-active sites while the ion transport lengths were greatly reduced for the porous structure (denoted as MP-Ti_3C_2). The capacitance and rate ability of MP-Ti_3C_2 have been significantly improved compared to HG-Ti_3C_2 (Figure 12d).

Fan *et al.* recently implemented another sacrificial template method to prepare a freestanding and flexible mesoporous $Ti_3C_2T_x$ film by mixing $Fe(OH)_3$ nanoparticles with $Ti_3C_2T_x$ and removing the $Fe(OH)_3$ by HCl, followed by calcination at 200 °C to remove some terminal groups of $Ti_3C_2T_x$.[64] This generates a highly interconnected nanopore channel to promote ion transport efficiently without sacrificing its ultrahigh density. In contrast to pure $Ti_3C_2T_x$ films, the mesoporous $Ti_3C_2T_x$ films maintained a high channel connectivity as well as a typical layer structure without deteriorating its superior mechanical flexibility. The porous $Ti_3C_2T_x$ films showed a specific capacitance of 346 F g^{-1} at 0.5 A g^{-1} while the original films achieved 288 F g^{-1} at the same current density. Due to the high density of the porous $Ti_3C_2T_x$ film (3.3 g cm^{-3}), it exhibited a high volumetric capacitance up to 1,142 F cm^{-3}.[64] When the current density was 20 A g^{-1}, the volumetric capacitance of modified mesoporous films could still maintain as high as 828 F cm^{-3} (72.5% retention) while pure $Ti_3C_2T_x$ films only possessed a capacitance retention of 45.8%.[64] There are also other methods to fabricate porous MXene films. Li *et al.* prepared

foam-like macroporous $Ti_3C_2T_x$ films featuring numerous macropores on the surface layer and a complex open 3D inner-architecture by heating a $Ti_3C_2T_x$/urea composite at 550 °C under argon atmosphere.[143] The obtained 3D structure had a drastic impact on improving the ion transport capabilities of the materials and sites available for electrolytic ions. A gravimetric capacitance of 203 F g^{-1} has been achieved at 5 A g^{-1}, which is much higher that the stacked $Ti_3C_2T_x$ films (80 F g^{-1}).[143]

Thick electrodes with high areal capacitance are essential due to the restricted area of devices for practical applications. However, it is quite difficult to increase the areal capacitance proportionately for film-based electrodes, as found in other reports.[64, 144, 145] The reason for this variation is that increasing the thickness of film electrodes will lead to the increased transport resistance.[88, 146] Assembling 2D nanoscale building blocks into 3D porous structure have been demonstrated to be of great significance to achieve high areal capacitance.[49] Wang *et al.* reported the design of a 3D porous $Ti_3C_2T_x$/bacterial cellulose (BC) freestanding film.[56] As displayed in Figure 12e, the nano-wall was assembled by netlike or intertwined fibers and interconnected nanosheets, which resulted in improved mechanical properties and continuous conductive path. Besides, BC also played a role in inhibiting the self-stacking of $Ti_3C_2T_x$ by fiber skeleton supporting between $Ti_3C_2T_x$ nanosheets and reacted with $Ti_3C_2T_x$ to form a well-defined architecture like honeycomb (Figure 12f). These factors contributed to the ultrahigh capacitance performance (416 F g^{-1}, 2,084 mF cm^{-2} at 3 mA cm^{-2}) at a relatively high areal mass loading of 5 mg cm^{-2}.[56] As shown in Figure 12g, there is a linear relationship between $Ti_3C_2T_x$ mass loading and areal capacitance, indicating that the unfavorable influence brought from increasing thickness can be alleviated by creating 3D porous structure, which is a desirable effect for energy storage systems.

It is worth noting that too many pores in 3D porous structure may result in relatively low volumetric specific capacity (low density) and easy oxidation of MXene flakes, which are

35

disadvantageous for wearable devices. The introduction of other nanomaterials with MXenes has been also considered for further improving the volumetric and areal performance of flexible $Ti_3C_2T_x$ electrodes. The selection of suitable nanomaterials is the key to meet the ever-growing energy demand for the evolution of electronic systems.[147] Recently, 1D MnO_2, as a high-performance pseudocapacitive filler, has been reported for $Ti_3C_2T_x$-based supercapacitor electrodes. $Ti_3C_2T_x$/MnO_2 hybrid film was synthesized through solution processing of hybrid inks of ultralong MnO_2 nanowires (NWs) and $Ti_3C_2T_x$ flakes (Figure 12h).[36] In the hybrid film, MnO_2 NWs served as the interlayer spacers to prevent the restacking of MXene flakes and added an additional electrochemically active material between the $Ti_3C_2T_x$ nanosheets, which improved the pseudocapacitance while maintaining the outstanding flexibility of the composite films (Figure 12i). The $Ti_3C_2T_x$/MnO_2 hybrid films showed an areal capacitance of up to 205 $mF\ cm^{-2}$ and delivered outstanding volumetric capacitance of up to 1,025 $F\ cm^{-3}$ at 1 $A\ cm^{-3}$ (Figure 12j).[36] In contrast, the pure $Ti_3C_2T_x$ and MnO_2 films merely delivered inferior specific areal capacitance of 52.5 and 39.4 $mF\ cm^{-2}$ and specific volumetric capacitances of 262.5 and 197.0 $F\ cm^{-3}$, respectively.[36]

Surface modification has also been proven to effectively enhance the volumetric capacitance of $Ti_3C_2T_x$ films.[148, 149] It has been reported that the alkalinizing process made –F terminal groups being selectively replaced by easily removed –OH, as Ti–F bonds became unstable in the basic solution.[150, 151] The annealing treatment resulted in the removal of surface groups, the increment of the exposed redox-active sites, and the increased crystalline order of $Ti_3C_2T_x$. Liu *et al.* synthesized surface modified $Ti_3C_2T_x$ films through alkalization and annealing (the resulting films was denoted as ak-$Ti_3C_2T_x$ films).[145] From Figure 12k, it can be seen that the typical layer structure of $Ti_3C_2T_x$ maintained well after the successive modifications. The ak-$Ti_3C_2T_x$ film showed an ultrahigh volumetric capacitance up to 1,805 $F\ cm^{-3}$ at 1 $A\ g^{-1}$, and the corresponding capacitance retention is 70% at 20 $A\ g^{-1}$ (Figure 12l).[145] The volumetric capacitance of this modified $Ti_3C_2T_x$ film is much higher than many $Ti_3C_2T_x$-based composite

films, which indicates that there is still much room to improve the electrochemical properties of $Ti_3C_2T_x$ films by surface chemistries.
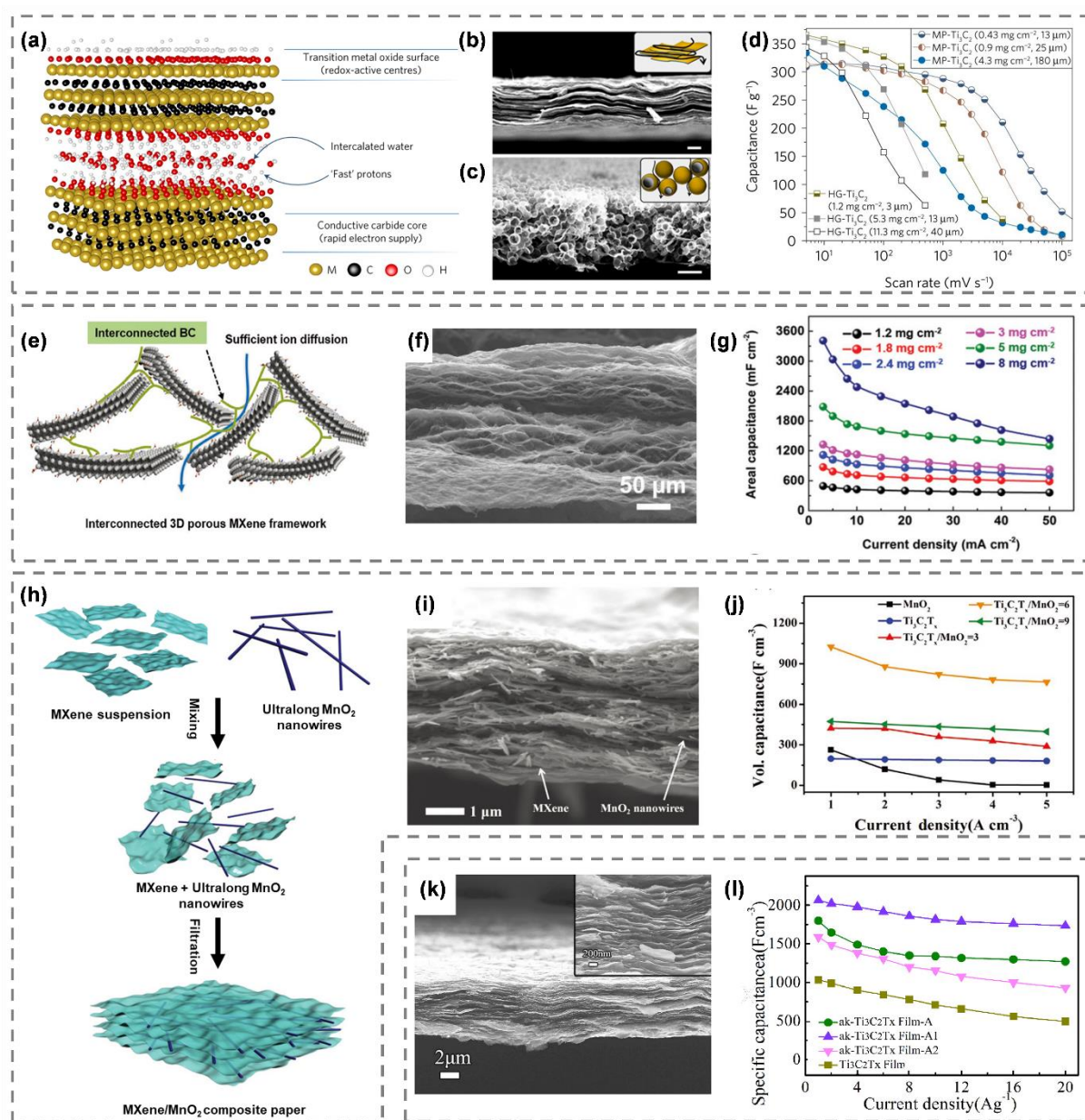
Figure 12. (a) Schematic illustration of MXene unique structure. Cross-sectional SEM images of $Ti_3C_2T_x$ with (b) layered stack and (c) porous structure. (d) Rate performance of $Ti_3C_2T_x$ films with different structure and mass loadings. Reproduced with permission.[66] Copyright 2017, Nature Publishing Group. (e) Formation process and photograph display of $Ti_3C_2T_x$/BC composites. (f) Cross-sectional SEM images of $Ti_3C_2T_x$/BC composites. (g) Areal capacitance of $Ti_3C_2T_x$/BC composites at current densities varying from 3 to 50 mA cm^{-2}.[56] Reproduced with permission.[56] Copyright 2019, Wiley. (h) Schematic representation of fabrication process of $Ti_3C_2T_x$/MnO$_2$ hybrid films. (i) Cross-sectional SEM image of $Ti_3C_2T_x$/MnO$_2$ hybrid films. (j) Specific volumetric capacitance of different samples at current densities varying from 1 to 5 A cm^{-3}. Reproduced with permission.[36] Copyright 2018, Wiley. (k) Cross-sectional SEM images of modified ak-$Ti_3C_2T_x$ films. (l) The specific capacitance of different samples versus current density. Reproduced with permission.[145] Copyright 2019, Elsevier.

While conventional supercapacitors are too large for the microdevices, microsupercapacitors are considered to be an attractive choice for wearable or miniaturized electronic devices, especially for integrated and self-powered smart devices. The performance of microsupercapacitors is more dependent on normalizing energy and power density in a given footprint area.[152] Because of the high volumetric capacitance, extremely high electrical conductivity and outstanding flexibility, MXene-based films are particularly suitable for microsupercapacitors.[153] A controllable deposition of MXene flakes method is the key step to construct MXene-based film electrodes for microsupercapacitors. Recently, Kurra *et al.* employed a simple, scalable and low-cost strategy to deposit $Ti_3C_2T_x$ films.[154] $Ti_3C_2T_x$ slurry was coated on commercial printing paper through the use of a Meyer rod. Then they utilized laser machining to fabricate $Ti_3C_2T_x$ coplanar films electrodes on the economical printing paper substrates over a large area (**Figure 13**a). The flexible $Ti_3C_2T_x$/paper electrodes offer more possibilities for the fabrication of energy storage devices by engraving with from simple scissors to more precise laser machining. The authors used two different etchants to synthesize $Ti_3C_2T_x$ slurry, one was HF, another was the mixture of HCl and LiF (the obtained MXene denoted as clay-like $Ti_3C_2T_x$). The areal capacitance of both HF-etched and clay-like $Ti_3C_2T_x$ at different scan rates have tested. It has been found that the clay-like Ti_3C_2 exhibited four times higher capacitance than HF-etched $Ti_3C_2T_x$ due to the larger interlayer spacing caused by the intercalation of water and Li^+ (Figure 13b). [88, 154]

3D printing is an emerging technology in recent years. Zhang *et al.* combined 3D printing with the superior physicochemical property of $Ti_3C_2T_x$ to fabricate coplanar all-$Ti_3C_2T_x$ microsupercapacitors.[98] The $Ti_3C_2T_x$ ink was uniformly brushed on the rough surface of the stamp 3D-printed by computer-aided design, which was then firmly pressed onto proper substrates such as printing paper. Solid-state $Ti_3C_2T_x$-based microsupercapacitors were finally successfully made after attaching Ag wires and casting the gel electrolyte (Figure 13c–f). As

seen in Figure 13g, the $Ti_3C_2T_x$ ink-based microsupercapacitors on paper were very flexible, which could maintain an efficient conductive network (conductivity changes < 15%) upon repeated bending/releasing.[98] Besides, the thickness of the finger electrode, the number of fingers and finger gaps could be easily tuning by brushing more $Ti_3C_2T_x$ ink on the stamps and changing the shape of the stamps. It has been found that increasing the numbers of fingers and electrode thickness or decreasing the finger gaps led to the improvement of areal capacitance. Under optimal conditions, the interdigitated $Ti_3C_2T_x$ microsupercapacitors exhibited high areal capacitance up to 61 mF cm^{-2} at 25 μA cm^{-2} (Figure 13h).[98]

It should be emphasized that the preparation of thick $Ti_3C_2T_x$ film electrodes is in favor of manufacturing microsupercapacitors with high specific areal capacity. In this context, Hu *et al.* presented a strategy to conveniently prepare thick $Ti_3C_2T_x$ film electrodes via bonding modularized thin $Ti_3C_2T_x$ films (fabricated by vacuum-assisted deposition) which consist of fully delaminated few-layered $Ti_3C_2T_x$ flakes only with water.[155] The thickness of the resulting films could be easily tuned by adding the number of superposed modularized thin $Ti_3C_2T_x$ films, like high wall made of standard thickness bricks. As compared to the traditional time-consuming vacuum-assisted deposition, this method could simply obtain thick $Ti_3C_2T_x$ film electrodes with the precise control of the corresponding thickness. Followed by common laser-cutting pattern process, on-chip microsupercapacitors reached a maximal areal capacitance of 71.16 mF cm^{-2} and a maximal energy density of 3.52 μWh cm^{-2}.[155]
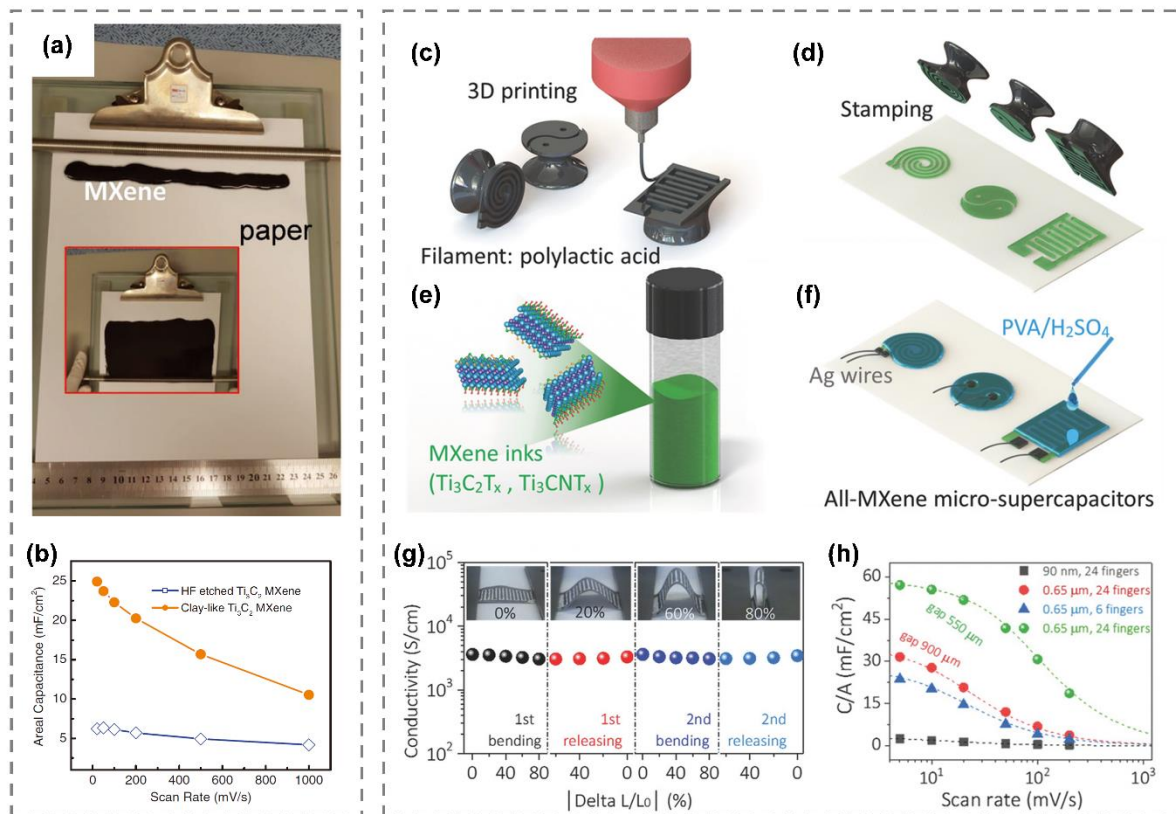
Figure 13. (a) $Ti_3C_2T_x$ slurry on an A4 printing paper with Meyer rod (inset demonstrates the coating process). (b) Areal capacitance of two samples versus scan rate. Reproduced with permission.[154] Copyright 2016, Wiley. (c-f) Fabrication of all-MXene-based microsupercapacitors using the stamping strategy. (g) Conductivity changes as a function of bending degree of $Ti_3C_2T_x$ ink on paper (insets are photographs of bending device). (h) Areal capacitances of $Ti_3C_2T_x$ with various configurations. Reproduced with permission.[98] Copyright 2018, Wiley.

In summary, various protocols have been developed to fabricate $Ti_3C_2T_x$-based films for electrochemical lithium/sodium-ion storage and supercapacitors, such as the construction of 3D structures by using templates of spacers, the introduction of electrochemically active materials, and controlling the film formation process (**Table 2**). Future fabrication techniques of MXene films for lithium-/sodium-ion storage and capacitor techniques could potentially improve the electrochemical and capacitive performances through designed architectures of MXene films.

Table 2. Summary of $Ti_3C_2T_x$-based films for lithium-/sodium-ion storage and supercapacitors.

Material	Device	Feature	Electrochemical performance	Film forming methods	Ref.

$Ti_3C_2T_x$/CNT	Na-ion storage	Introduction of CNTs as spacer	175 mA h g^{-1} at 0.1 A g^{-1}	Filtration	[117]
$Ti_3C_2T_x$/Si	Li-ion storage	Introduction of Si	2,118 mA h g^{-1} at 0.2A g^{-1} after 200 cycles	Filtration	[139]
$Ti_3C_2T_x$/rGO	Li-ion storage	Crosslinked 3D structure	335.5 mA h g^{-1} at 0.05 A g^{-1}	Filtration	[83]
$Ti_3C_2T_x$	Na-ion storage	Using PMMA to construct 3D structure	330 mA h g^{-1} at 0.25 C	Filtration	[96]
$Ti_3C_2T_x$	Supercapacitor	Using $Fe(OH)_3$ to construct 3D structure	346 F g^{-1} at 0.5 A g^{-1}	Filtration	[64]
$Ti_3C_2T_x$	Supercapacitor	Using urea to construct 3D structure	203 F g^{-1} at 5 A g^{-1}	Filtration	[143]
$Ti_3C_2T_x$/BC	Supercapacitor	Using BC to construct 3D structure	416 F g^{-1} at 3 mA cm^{-2}	Filtration	[56]
$Ti_3C_2T_x$/MnO$_2$	Supercapacitor	Introduction of 1D MnO_2 as spacers	205 mF cm^{-2} at 1 A cm^{-3}	Filtration	[36]
$Ti_3C_2T_x$	Supercapacitor	Surface modification	1,805 F cm^{-3} at 1 A g^{-1}	Filtration	[145]
$Ti_3C_2T_x$	Supercapacitor	Novel film forming method	25 mF cm^{-2} at 20 mV s^{-1}	Slurry coating	[154]
$Ti_3C_2T_x$	Supercapacitor	Novel film forming method	61 mF cm^{-2} at 25 μA cm^{-2}	Stamping strategy	[98]
$Ti_3C_2T_x$	Supercapacitor	Novel film forming method	71.16 mF cm^{-2} at 1 mA cm^{-2}	Sectionalized filtration	[155]

3.3. Transparent conductive electrodes

Transparent conductive electrodes (TCEs), with a combination of high transparency and electrical conductivity, are critical components in the optoelectronic devices, such as solar cells, liquid-crystal displays, sensors, and touch panels.[156] As the combination of the remarkable optical performance and ultrahigh conductivity, MXenes afford a great potential for TCEs. Solution-based technology, such as spray-coating, spin-casting, dip-coating, electrophoretic deposition, vacuum filtration, is a more appropriate method to obtain high quality transparent conductive MXene films for large-scale and cost-effective applications. Among them, spin-coating can produce compact and uniform $Ti_3C_2T_x$ on the flat substrate effectively. For example, Marina *et al.* demonstrated the preparation of conductive $Ti_3C_2T_x$ films via spin-coating process.[68] As demonstrated in **Figure 14**a, with slower spin rate, more $Ti_3C_2T_x$ flakes tend to

41

be deposited and overlapped. The film thickness could be conveniently controlled by varying the speed, duration and concentration of the solution. It was demonstrated that the films deposited at 400 rpm possessed the sheet resistances (R_{sh}) of 437 Ω/sq (Ω/sq is the unit of sheet resistance) with a transparency of 77%.[68] As compared to the high resistances (1,000 Ω/sq) of rGO with the same transparency, these spin-coating films of $Ti_3C_2T_x$ performed better while reducing their R_{sh} by about the half (Figure 14b).[68]

Homogeneous transparent conductive films could be produced on various substrates over large areas by spray-coating. Kanit *et al.* used the colloidal delaminated $Ti_3C_2T_x$ solution to fabricate transparent conductive thin films by spray coating (Figure 14c).[108] This method could deposit $Ti_3C_2T_x$ flakes on large areas, up to a letter-size paper sheet or larger. The transmittance gradually decreased with the increased thickness but still remained 43.8% at a thickness of 70 nm (Figure 14d).[108] For quantitative comparison of transparent conductors, a common figure of merit (FOM), defined as the ratio of the DC conductivity (σ_{DC}) to optical conductivity (σ_{OP}) derived from the optical transmittance, is used to evaluate the optoelectronic properties. The FOM of the thin $Ti_3C_2T_x$ made by spray-coating was in the range of 0.5-0.7.[108]

In order to acquire high FOM and further reduce the sheet resistance to be comparable to that of ITO, Yang *et al.* studied Ti_2CT_x films, another type of MXene, as a TCE.[156] By dip-coating of an Al_2O_3 substrate in a colloidal solution of Ti_2CT_x thin flakes, they fabricated the homogeneous transparent conductive thin films. The sheet resistance was as low as 70 Ω/sq at 86% transmittance, which corresponded to the high FOM of 40.7,[156] while that of solution-processed $Ti_3C_2T_x$[108] and rGO[157, 158] were about 3.1 and 1.6, respectively. Furthermore, the thickness of the film was tuned by a SF_6+Ar plasma treatment, which etched Ti_2CT_x film layer-by-layer and removed the top oxidized layer without affecting the bottom layer of the Ti_2CT_x flake. The plasma-treated Ti_2CT_x film exhibited the single-crystalline structure with few intrinsic defects due to the elimination of surface terminal groups and impurities after the plasma treatment.[159] The resistivity of plasma-treated (100 s) Ti_2CT_x film was further

decreased to 63 Ω/sq with an improved transmittance of 89% and FOM of 51. (Figure 14e).[156]

However, dip-coating required multiple steps, which made it time-consuming for the

fabrication of MXene-based films.
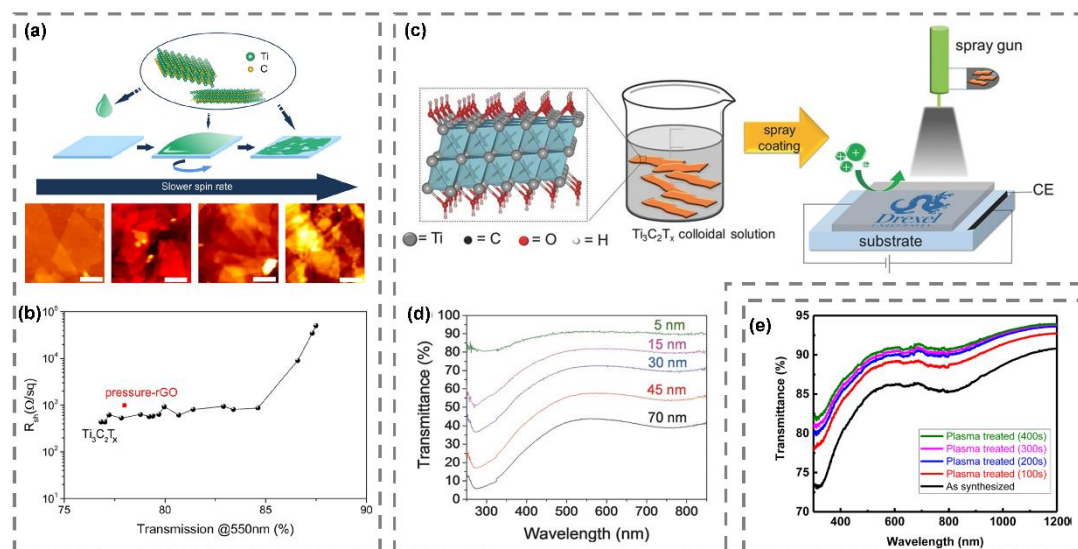
Figure 14. (a) Diagram showing how substrates are coated using a solution containing delaminated $Ti_3C_2T_x$ flake. (b) Measured sheet resistance as a function of film transmission at 550 nm. Reproduced with permission.[68] Copyright 2016, Royal Society of Chemistry. (c) Schematic of $Ti_3C_2T_x$ film preparation by spray coating. CE presents counter electrode. (d) UV–vis spectra of $Ti_3C_2T_x$ films with different thicknesses. Reproduced with permission.[108] Copyright 2016, Wiley. (e) Transmission spectra of Ti_2CT_x film with different plasma etching time. Reproduced with permission.[156] Copyright 2017, American Chemical Society.

3.4. Water purification

There is an urgent need for developing reliable technologies for water purification that can

effectively remove the impurities from water, such as heavy metal ions and soil droplets. With

low-level chemical requirement, high removal efficiency, and reduced carbon footprint,

membrane separation and purification are an economical, safe, effective and reasonable

treatment process, which have been extensively employed in the chemical, pharmaceutical, and

water industries.[5] Different cations, such as Na^+, K^+, Mg^{2+}, and Al^{3+},[160] and various kinds of

organic molecules such as hydrazine, urea and dimethyl sulfoxide,[103] can intercalate $Ti_3C_2T_x$

sheet spontaneously, which indicates that MXene could potentially serve as adsorbents.[100] In

addition, surface termination groups of MXene may play a special role in water purification.

43

For example, –OH can facilitate the reduction of heavy mental ions.[77] Besides, to achieve high-efficient and rapid water purification, the separation films should meet the following two criteria: special wettability to water, and suitable pore size. In this context, MXene-based films combining the inherent hydrophilicity of MXene with the potential toward tunable pore sizes, is quite suitable for water purification while the combination of these capabilities is rarely present synchronously in a material.[161]

Pandey et al. fabricated anti-fouling Ag@$Ti_3C_2T_x$ composite-based films by vacuum-assisted filtration after direct reduction of $AgNO_3$ on the surface of $Ti_3C_2T_x$, where $Ti_3C_2T_x$ acted as films matrix and reducing agent.[161] From **Figure 15**a and b, we could clearly see the typical layered structure and the successful introduction of Ag nanoparticles. As an increase in the proportion of Ag nanoparticles, the pure water flux increased. The improvement in water flux can be attributed to short transport pathway and formation of voids due to the pillaring of Ag nanoparticles on $Ti_3C_2T_x$ surface. Furthermore, the water contact angle decreased from 39.5° to 35.0° with increasing Ag nanoparticles content from 0 to 21%, which indicates the positive influence of Ag nanoparticles on the surface hydrophilicity. As a consequence of the optimization of structure and hydrophilicity, rhodamine B (RhB,79.9%), methyl green (MG, 92.3%), and bovine serum albumin (BSA, > 99%) were effectively removed (Figure 15c). With an average pore size of 2.1 nm, the Ag@$Ti_3C_2T_x$ films demonstrated more than 4 times of the water flux (~420 L m^{-2} h^{-1} bar^{-1}) than the pure $Ti_3C_2T_x$ films (~118 L m^{-2} h^{-1} bar^{-1}), during RhB, MG, and BSA rejection (Figure 15d).[161] However, the rejection of MG and RhB were slightly less than those of the pure $Ti_3C_2T_x$ films due to the their more open structure.

Template method is also promising for enhancing the water permeability of MXenes-based films for water purification. For instance, using $Fe(OH)_3$ as a sacrificial template to create expanded nanochannels, Ding *et al.* fabricated a 2D lamellar $Ti_3C_2T_x$ film on an anodic aluminum oxide support by vacuum filtration with superhigh water permeability (> 1,000 L m^{-2} h^{-1} bar^{-1}).[162] The water permeability of the film was approximately ten-fold higher than that

of commercial polyethersulfone films with nominal molecular weight cut-offs of 30 kDa and 50 kDa (< 150 L m^{-2} h^{-1} bar^{-1}). The Ti$_3$C$_2$T$_x$ films excluded nearly 100% of BSA and gold nanoparticles (5 nm), 90% Evans blue (1.2×3.1 nm^2), 85% RhB (1.8×1.4 nm^2), but small molecules (< 1 nm) such as K$_3$[Fe(CN)$_6$] (0.9 nm × 0.9 nm) was not readily removed (32% only).[162] These results indicated that the pore size of the Ti$_3$C$_2$T$_x$ films was around 2–5 nm, which limits its permeation and rejection properties. In order to further improve the liquid permeability and rejection efficiency, Wang *et al.* chose well-delaminated Ti$_3$C$_2$T$_x$ as rigid building blocks to obtain a unique 2D lamellar membrane with an exceptional performance.[111] As demonstrated in Figure 15e, the Ti$_3$C$_2$T$_x$ films readily achieved an unparalleled water permeance in solvated state (2,302 L m^{-2} h^{-1} bar^{-1}), 9 times of that measured of GO (257 L m^{-2} h^{-1} bar^{-1}).[111] The ultrahigh permeance should be mainly ascribed to the ordered, straight and lamellar interlayer channels. With the structural advantages, the films exhibited high-level removal rates, *i.e.*, ~100% for acid yellow 79 (AY19, 2.8 nm), 96% for reactive black (RB, 2.0 nm), and ~56% for acid yellow 14 (AY14, 1.9 nm) (Figure 15f). It remains a challenge to reject molecules with a size smaller than 2.0 nm for Ti$_3$C$_2$T$_x$-based films, such as helianthin B (1.2 nm, with rejection of 32%).

Xie *et al.* reported the Ti$_3$C$_2$T$_x$/rGO hybrid films for pressure-free removal of multiple negatively and positively charged heavy mental ions (HMIs) from water, such as HCrO$_4^-$, AuCl$_4^-$, PdCl$_4^{2-}$, and Ag$^+$, via redox reactions, surpassing the principles of electrostatic attraction or coordination chemistry, which only selectively removed HMIs.[77] The introduction of rGO effectively mitigated the restacking tendency of Ti$_3$C$_2$T$_x$, facilitating rapid mass transfer across the interface of the Ti$_3$C$_2$T$_x$-based films.[77] With further treatment in HCl solution for surface hydroxylation, the surface-modified films (denoted as HRM) showed a much lower water contact angle of 64.7° than pure Ti$_3$C$_2$T$_x$ film (PM) and rGO-intercalated Ti$_3$C$_2$T$_x$ film (RM).[77] In addition, the increased content of –OH on Ti$_3$C$_2$T$_x$ also facilitated the reduction of HMIs through enhancement of adsorption and charge transfer from Ti$_3$C$_2$T$_x$ to

HMIs.[77] The combination of microstructure optimization and control of surface properties of MXene/rGO hybrid films leaded to the enhanced removal of multifarious HMIs from water under pressure-free conditions, and removal capacities for Cr(VI), Pd(II), Au(III) and Ag(I) were 84, 890, 1241 and 1,172 mg g^{-1}, respectively, much higher than that of PM and RM as shown in Figure 15g–j.[77]
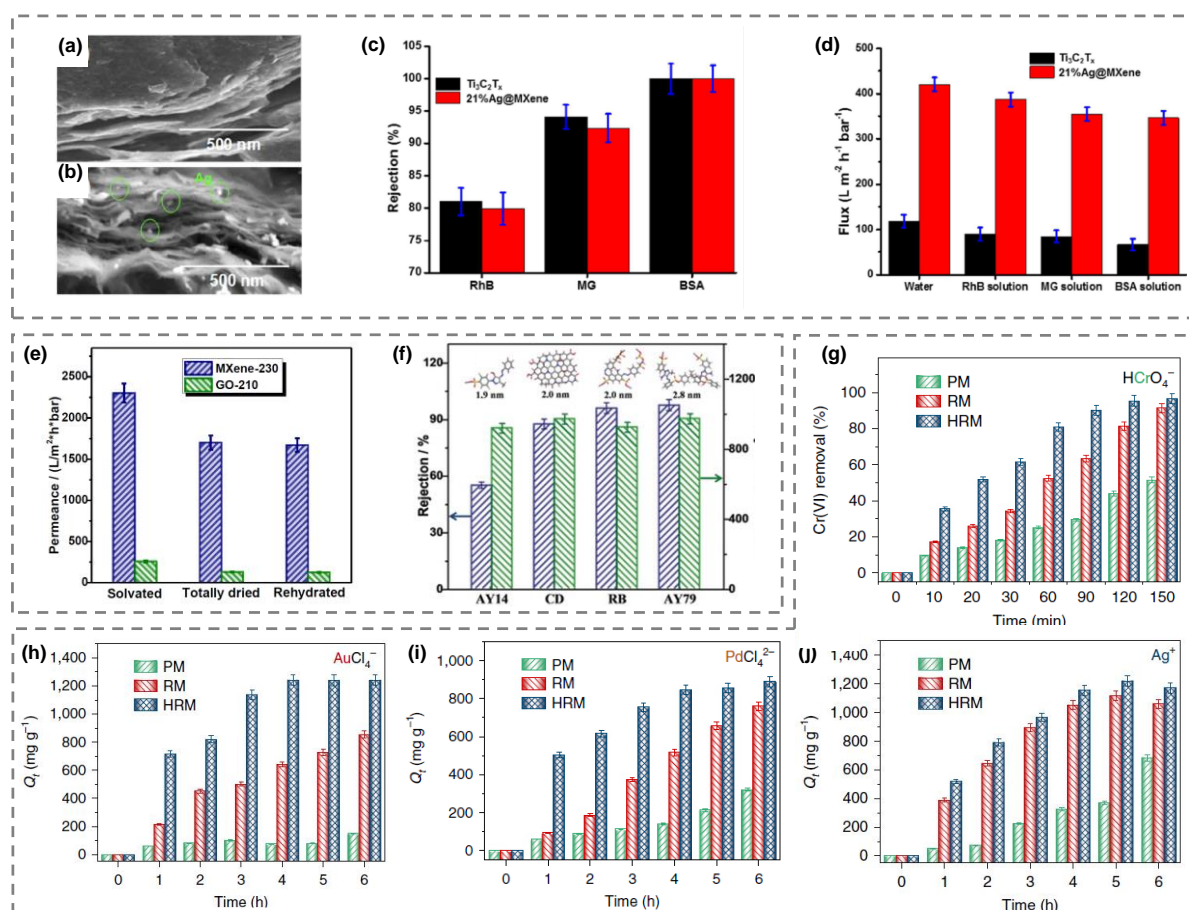
Figure 15. SEM cross-section images of (a) $Ti_3C_2T_x$ and (b) 21%Ag@$Ti_3C_2T_x$ films. (c) Rejection and (d) flux of the pure $Ti_3C_2T_x$ and 21%Ag@$Ti_3C_2T_x$ films during the separation of RhB, MG and BSA molecules at 25 °C. Reproduced with permission.[68, 161] Copyright 2018, Royal Society of Chemistry. (e) Water permeance of $Ti_3C_2T_x$ and GO films in solvated, totally dried, and rehydrated states. (f) Separation performance of the $Ti_3C_2T_x$ films for molecules with different sizes. Reproduced with permission.[111] Copyright 2018, John Wiley & Sons, Inc. Time-online profiles for removal of (g) $HCrO_4^-$, (h) $AuCl_4^-$, (i) $PdCl_4^{2-}$ and (j) Ag^+ over PM, RM and HRM films under pressure-free conditions. Reproduced with permission.[77] Copyright 2019, Nature Publishing Group.

3.5. Electromagnetic interference (EMI) shielding

In addition to the aforementioned applications, MXene-based films have outstanding performances in electromagnetic interference (EMI) shielding and sensors.[37, 163-165] EMI is becoming a troublesome problem in the design of electronic devices, as EMI has detrimental impacts on device performance, and the lifetime of the electronic equipment. Hence, the investigation and application of EMI shielding materials are crucial to solve this problem.[76] Recently, many carbon-based materials (e.g., graphene,[166] rGO,[167] and carbon black[168]) were reported for EMI shielding applications. However, 2D MXenes exhibit superior EMI shielding property and have been proved to be promising candidates as EMI shielding materials.[169] In detail, outstanding electrical conductivity brought from $Ti_3C_2T_x$ flakes and multiple internal reflections within the nacre-like (or laminated) structure endowed the $Ti_3C_2T_x$ films with excellent EMI shielding effectiveness (>50 decibels for a 2.5-µm-thick film).[62] The EMI shielding mechanism was clarified as follows: as electromagnetic waves struck the surface of a $Ti_3C_2T_x$ flake, some of the waves are immediately reflected because of abundant free electrons on $Ti_3C_2T_x$.[62] The remaining electromagnetic waves, after going through the first layers of $Ti_3C_2T_x$ would reach the next $Ti_3C_2T_x$ flakes as barrier layer and the phenomenon of electromagnetic wave attenuation repeated (**Figure 16**a). Hence, the laminated structure enabled $Ti_3C_2T_x$ with the multilevel shield, which was a tremendous advantage in contrast to materials with no interlayer reflecting surface.

Additionally, MXene/polymer films are currently emerging for EMI shielding due to the low percolation threshold, enhanced mechanical properties, high temperature resistance and excellent shielding efficiency.[170, 171] For example, Shahzad *et al.* fabricated $Ti_3C_2T_x$/polymer composite films by vacuum assisted filtration of $Ti_3C_2T_x$ and sodium alginate (SA) colloidal solutions.[62] The introduction of SA could effectively separate the $Ti_3C_2T_x$ flakes, maintain the strong mechanical properties, and even add oxidation resistance. Materials with high electrical conductivity are typically preferable to obtain high EMI shielding effectiveness values (57 dB for a 26-µm-thick hybrid film). However, SA lacks high conductivity (far less than 1 S cm⁻

^{1}).[172] Consequently, as $Ti_3C_2T_x$ content increased, electrical conductivity of the composited films increased rapidly, which further demonstrated that the addition of $Ti_3C_2T_x$ is effective to add electrical conductivity to the polymer composite (Figure 16b). In later research, Zhou *et al.* obtained $Ti_3C_2T_x$/calcium alginate (CA) aerogel films with sponge-like structure by simply crosslinking SA molecules with calcium ions.[173] Due to the advantages of the structure and morphology characteristics, the $Ti_3C_2T_x$/CA aerogel films showed an excellent EMI SE (54.3 dB at the thickness of 26 μm), which was higher than that of pure $Ti_3C_2T_x$ and $Ti_3C_2T_x$/SA films under the same condition.[173]

Moreover, other nanomaterials have been used to improve MXenes' EMI performance. For example, Chen *et al.* fabricated MXene ($Ti_3C_2T_x$)/Ag nanowire (MA) films via a simple spray-coating technique and successfully achieved outstanding shielding performances while retaining high light transmittances.[174] The MA films prepared with m mg m^{-2} of $Ti_3C_2T_x$ and n mg m^{-2} of Ag nanowires (NWs) was denoted as $MA_{m/n}$. Compared to bare AgNWs film (21 dB), MA film with the same AgNWs loading exhibited much higher shielding performance (34 dB) with better mechanical properties and environmental stability.[174] In addition, a novel layered structure design was formed where a $MA_{2m/2n}$ film was equally divided to two thinner $MA_{m/n}$ films then superposed with a certain gap distance (Figure 16c), the EMI shielding performance was further improved to 49.2 dB without sacrificing its transmittance (retain ~83% transmittance).[174] Compared to the bulk MA film, the multi-layered MA films could attenuate microwave more effectively by additional reflection on the interior interfaces.
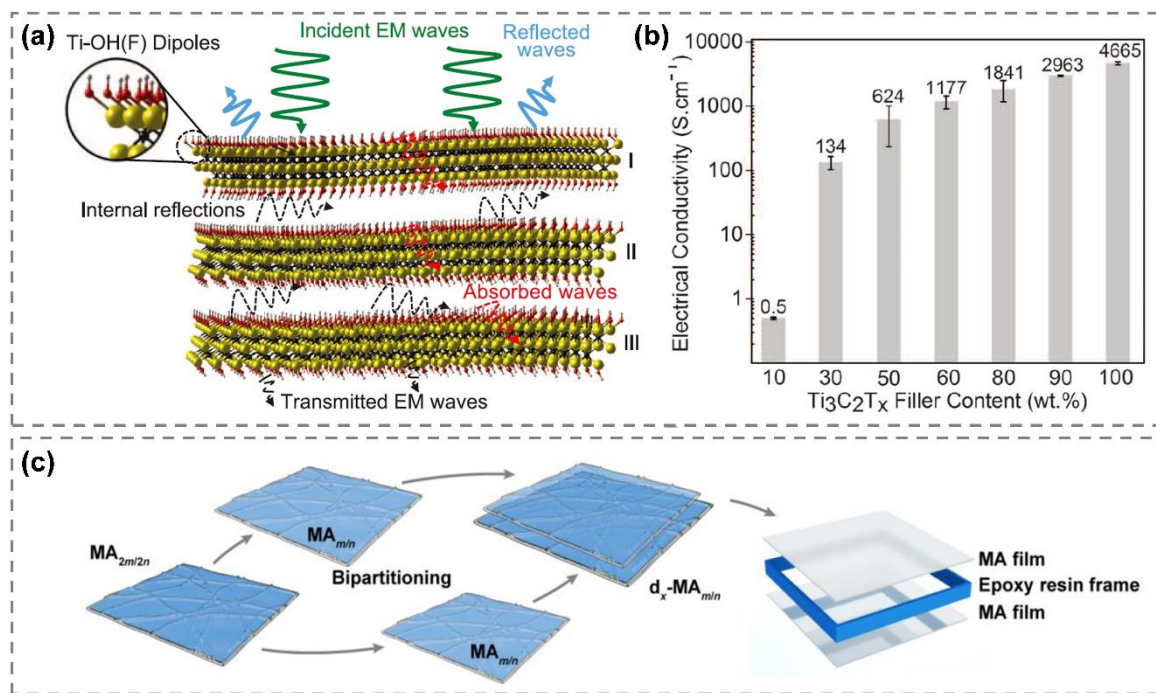
Figure 16. (a) Schematic diagram of proposed EMI shielding mechanism of $Ti_3C_2T_x$-SA composite films. (b) Electrical conductivity of $Ti_3C_2T_x$-SA composites with filler content variation. Reproduced with permission.[62] Copyright 2016, American Association for the Advancement of Science. (c) Schematic illustration of preparation process of MA film. Reproduced with permission.[174] Copyright 2020, American Chemical Society.

3.6. Other applications

MXene-based films can also work as sensors to detect the change of external conditions with high accuracy. For instance, MXene films can be used as gas sensors to detect different traces gas based on the principle that when electrons transfer from adsorbed gas to $Ti_3C_2T_x$, the concentration of majority charge carrier of the $Ti_3C_2T_x$ film decreases in the meantime, resulting in resistance increments in the $Ti_3C_2T_x$ device.[175] Lee *et al.* deposited $Ti_3C_2T_x$ on flexible polyimide films by a facile solution casting method and then fabricated corresponding sensors. The $Ti_3C_2T_x$ sensors successfully detected volatile organic compound gases such as ethanol, methanol, acetone, and obtained highest response for ammonia due to its large absorption energy. The limit of detection of acetone gas was theoretically calculated to be about 9.27 ppm, presenting a comparable performance to other 2D material-based sensors.[176, 177]

Beyond gas sensors, MXenes films have been explored as strain sensors as well. An *et al.* have synthesized $Ti_3C_2T_x$/diallyldimethylammonium chloride (PDAC) films strain sensors by

layer-by-layer (LBL) assembly technique (**Figure 17**a),[178] which showed excellent performance for detecting objects deformation. The resistance increased upon bending and stretching due to the formation of microcracks, which recovered after the release of external pressure. Significantly, the constructed sensor could precisely map the complex shapes as well as detect the angle of a bent index finger with high sensitivity, which may play a big role in the next generation of wearable devices (Figure 17b and c).
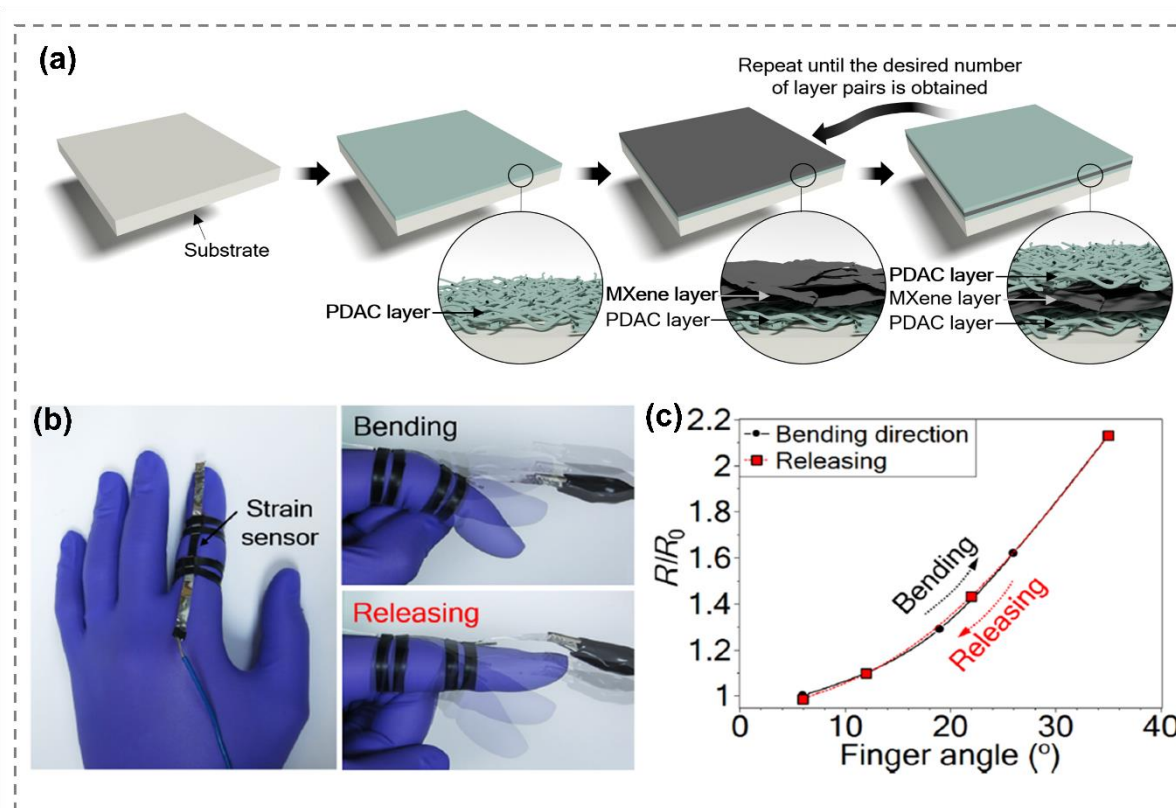
Figure 17. (a) Characterization of MXene/polyelectrolyte multilayers assembled using the LbL technique. (b) Digital image of the human motion strain sensor. (c) Response to finger motion. Reproduced with permission.[178] Copyright 2018, American Association for the Advancement of Science.

Owing to the expansion of global energy requirement, triboelectric nanogenerator (TENG) has attracted much attention, which can simply produce the electricity from mechanical energy.[179-181] Recently, based on the superior electrical conductivity and highly electronegative surface of $Ti_3C_2T_x$, Jiang *et al.* reported a flexible $Ti_3C_2T_x$/PVA film as the negative friction layer of TENG and the positive friction layer is made of silk fibroin (SF).[182]

50

The optimized TENG shows significantly enhanced flexibility and durability with the help of PVA, and $Ti_3C_2T_x$ makes up for PVA's lack of electrical conductivity, which sets the stage for applying in flexible wearable device. The positive material is inclined to lose electrons while the trend of negative material is to attract the electrons. As a result, the charges will flow across the load to keep the energy balance, and the detailed working principle is shown in **Figure** 18a. The TENG is able to power over 45 LEDs with the work frequency of 10 Hz and the force of 10 N, and maintain the stable voltage output after over 124,000 bending cycles.[182] Furthermore, the authors integrate a single-electrode mode TENG and use human skin to replace SF as the electron donor, which can achieve real-time monitor of different kinds of human motion. For example, as displayed in Figure 18b, a TENG attached on the throat is capable to recognize the shallow and deep breathing as well as the speaking by the real-time voltage response with no external energy supply.

Due to their promising biocompatibility and tunable physicochemical property properties, the biomedical applications of MXenes are flourishing in recent years.[183, 184] Although the biocompatibility evaluations of MXenes family are still under progress, it is proved that $Ti_3C_2T_x$ has no adverse toxicological effect on the neuron and muscle activity of the zebrafish embryo model. The lethal concentration 50% (LC_{50}) of $Ti_3C_2T_x$ exceeds to 100 μg mL^{-1}, which indicates that $Ti_3C_2T_x$ could be classified in the "practically nontoxic" group according to the Acute Toxicity Rating Scale set by the Fish and Wildlife Service.[185] For specific application such as biosensing, $Ti_3C_2T_x$ were used to fabricate biologically compatible field-effect transistors, which could have label-free detection of neurotransmitters and real-time monitoring of spiking activity in primary hippocampal neurons.[186] The primary hippocampal neurons can be cultured well on the $Ti_3C_2T_x$ thin films (micropatterns) while primary neurons are highly fragile, reflecting the superior biocompatibility of $Ti_3C_2T_x$.

Recently, MXenes have shown possession of a unique and promising potential for light-to-heat conversion.[187] This behavior is promising for applications of MXene-based films for the

direct solar energy conversion, such as solar desalination and light-driven actuation. For example, Zhao *et al.* reported the solar desalination potential of the hydrophobic $Ti_3C_2T_x$-based film modified by trimethoxy(1H,1H,2H,2H-perfluorodecyl)silane (PFDTMS).[188] The modified $Ti_3C_2T_x$ film was employed in a solar desalination device, which could be self-floated on the seawater and block water along with dissolved salts due to the PFDTMS modified hydrophobic $Ti_3C_2T_x$ surface. Furthermore, the hydrophobic $Ti_3C_2T_x$ film successfully realized a solar steam conversion efficiency of 71% with solar evaporation rate of 1.31 kg m^{-2} h^{-1} and over 99.5% salt rejection rate for Ca^{2+}, Mg^{2+}, and Na^+. Considering the promising light-to-heat conversion ability and the biocompatibility of $Ti_3C_2T_x$, it can be widely used in multiple biomedical applications such as drug delivery, photoacoustic, photothermal therapy.[187] For example, concurrent diagnostic imaging and therapy has been reported for $Ti_3C_2T_x$ with the integration of GdW_{10}-based polyoxometalates.[189] The $GdW_{10}@Ti_3C_2T_x$ composite nanosheets offered hyperthermal treatment with magnetic resonance and computed tomography imaging guidance for tumor cells. In addition, a tumor was effectually eradicated without reoccurrence during the period of operation.

In addition, light-driven actuators are another interesting application based on the attracting light-to-heat conversion ability of $Ti_3C_2T_x$. Cao *et al.* coated a thin hydrophobic film composed of polydimethylsiloxane (PDMS) and $Ti_3C_2T_x$ modified by fluorinated alkyl silane on a filter paper.[190] When exposed to near-infrared irradiation (NIR) laser irradiation (808 nm), the temperature of PDMS/$Ti_3C_2T_x$ coated filter paper (denoted as PDMS/$Ti_3C_2T_x$ paper) increased fast from 23.2 to 54.3 °C in 10 s and reached to 116.6 °C within 3 min (Figure 18c). Based on the superior light-to-heat conversion ability of $Ti_3C_2T_x$, the PDMS/$Ti_3C_2T_x$ paper is driven to move rotationally under NIR laser irradiation due to the local temperature gradients (Figure 18d). Furthermore, Liu *et al.* showed a convenient strategy to fabricate a bilayer-structured actuator by depositing $Ti_3C_2T_x$ on low-density polyethylene (LDPE).[191, 192] LDPE possesses a

high coefficient of thermal expansion and low thermal conductivity of about 0.3 W m^{-1} K^{-1} while the thermal expansion of Ti$_3$C$_2$T$_x$ with a high thermal conductivity of about 55.2 W m^{-1} K^{-1} is negligible compared to LDPE.[193] Benefited from the inverse thermal properties of these two materials, the actuator can realize a certain period of motion under the stimulation of light. The simple light-actuated devices derived from photothermal Ti$_3$C$_2$T$_x$ is potential to manufacture the light-driven robots for cargo delivery.
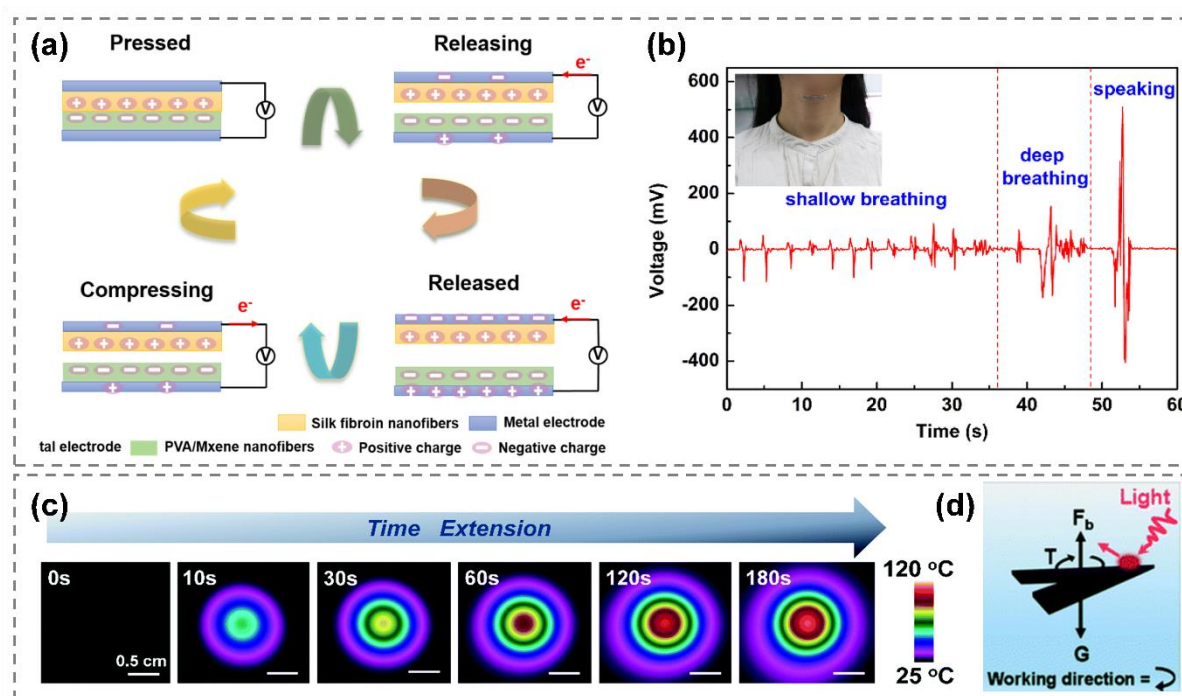
Figure 18. (a) Working mechanism of the TENG device. (b) The voltage changes of the device attached on throat muscle to reflect human activities. Reproduced with permission.[182] Copyright 2019, Elsevier. (c) Infrared thermographic photographs of the PDMS/Ti$_3$C$_2$T$_x$ paper under NIR irradiation at different time. (d) The illustration of the motion of PDMS/Ti$_3$C$_2$T$_x$ paper. Reproduced with permission.[190] Copyright 2019, Elsevier.

Besides the above-mentioned applications, MXene-based films have been reported other important fields such as fuel cells,[194] photocatalysis,[195, 196] electrocatalysis,[197, 198] solar cells,[199] antibacterial.[200] Through these examples, it is not hard to foresee the rapid development of MXene-based films with improved performance and their versatile applications.

4. Summary and outlook

The past several years have witnessed a rapid growth in both theoretical and experimental studies of $Ti_3C_2T_x$-based films on account of their unique properties.[13, 201] In this review, we introduce the competitive features, the fundamental properties and the engineering strategies of $Ti_3C_2T_x$-based films, which is expected to contribute to their further development. In addition, we have reviewed progress in the use of $Ti_3C_2T_x$-based materials for electrochemical lithium/sodium-ion storage, (micro-)supercapacitors, transparent conductive electrodes, water purification, EMI shielding and other applications. Improvement in each of these applications has been achieved by controlling the etching condition, elaborate structure design, doping, and surface modification. However, noticeable gaps between the academic research and the practical applications still exist in manufacture capability and device performance of $Ti_3C_2T_x$-based films. In an effort to narrow these critical gaps, here, we have analyzed key challenges and perspectives in manufacturing $Ti_3C_2T_x$-based functional films to facilitate the lab-to-industry translation.

Among different kinds of MXenes, $Ti_3C_2T_x$ has received the most attention, especially in energy storage and EMI shielding.[17] Notably, there are still opportunities and challenges for related future studies. In general, it has been proven that the quality of $Ti_3C_2T_x$ flakes directly correlates to the electrical conductivity and moderate and safe synthetic approaches are in great demand.[13] Although the LiF-HCl etching method is proved to be a relatively mild and high-yield method than HF etching with few nanometer-size defects in the obtained $Ti_3C_2T_x$ flakes,[13] the extra water and/or cations between the interlayers may impede their intrinsic properties. Meanwhile, after the etching process, the delamination and subsequent collection of multi-layered $Ti_3C_2T_x$ need to be further developed due to the unique performance of few- or mono-layer sheets and their important role on the properties of $Ti_3C_2T_x$-based films. In this regard, further efforts should be devoted to simplifying the whole synthesis process with safety and obtaining a low concentration of defects and large flake sizes of $Ti_3C_2T_x$.

However, the oxidation of MXene films is one of the key problems impeding their practical application. Despite the fact that assembly into films will highly improve the environmental stability of $Ti_3C_2T_x$ flakes, $Ti_3C_2T_x$-based films have a relatively low resistance to humid environments. The modification of the edges and the defective sites by chemical grafting while maintaining the in-plane physiochemistry of the $Ti_3C_2T_x$ film will be beneficial to enhance the durability of $Ti_3C_2T_x$-based films, which is the prerequisite to transfer their potentials to practical applications in the future. Assembling $Ti_3C_2T_x$ flakes into films will lead to the restacking of $Ti_3C_2T_x$ flakes, which can be detrimental on the performance in transport applications. We have introduced some practical and effective methods to avoid the tendency of restacking and more competitive strategies are expected to be found. It should be noted that the majority of previous studies focused on alleviating the face-to-face stacking of $Ti_3C_2T_x$ flakes. However, the lateral crosslinking of $Ti_3C_2T_x$ flakes in the films and methodologies for the controllable construction of vertically aligned pores have been less investigated, which is of great significance for electrochemical applications. In addition, the exploration of $Ti_3C_2T_x$-based films for other applications with great promise is very attractive. For example, due to their excellent ion transport and good cation selectivity, $Ti_3C_2T_x$-based films could be suitable for nanofluidic osmotic power generators, which would be a novel sustainable self-sufficient nanopower source.[202]

In addition to the above-mentioned aspects, $Ti_3C_2T_x$-based films face structural swelling in applications such as membrane separators and catalytic applications, which would weaken ion exclusion ability and destroy the integrity of $Ti_3C_2T_x$-based films.[203] The swelling effect of $Ti_3C_2T_x$-based films is due to the absorption of water molecules into the interlayer space due to MXenes' hydrophilic nature as well as salt penetration into the film structure when the film is immersed in aqueous solutions.[204, 205] To address the swelling issue, several strategies have been proposed, such as covalent cross-linking by polymer molecules,[206, 207] and encapsulation with epoxy.[208] However, these strategies would potentially compromise the attractive

55

properties of $Ti_3C_2T_x$ by blocking the functional accessibility. Alternatively, encapsulating $Ti_3C_2T_x$-based films within interconnected porous structures, such as porous graphene monoliths, is expected to buffer the swelling effect. Further in-depth research efforts should be devoted to understanding and addressing the swelling issue effectively to promote further development of $Ti_3C_2T_x$-based films toward related applications.

The design of $Ti_3C_2T_x$-based film materials should comprehensively consider various characteristics to meet the practical application demand. For example, the application of supercapacitors in daily life calls for the optimization of electrode density and gravimetric capacitance to gain the maximum volumetric capacitance. Nevertheless, for most supercapacitor electrodes, there is a trade-off between density and gravimetric capacitance. Nowadays, it is highly desirable to coordinate the trade-off between density and gravimetric capacitance to maximize the volumetric capacitance for micro-devices. From this perspective, microporous and mesoporous structures are more likely to result in higher volumetric capacitance while macropores will significantly decrease the density of $Ti_3C_2T_x$-based films,[96] ending up with unsatisfactory volumetric capacitance. In addition, surface modification and the introduction of 1D spacers such as MnO_2 nanowires and CNTs is quite promising to achieve high volumetric capacitances. For wearable and portable devices, the introduction of conductive polymer materials such as PANI can serve as an effective strategy to balance the mechanical property and electrochemical performance for wearable devices. It should also be noted that the reported capacitances are obtained under the low mass loading of the active material. However, for most energy storage devices, the capacitance does not scale linearly with electrode thickness or mass loading, which is challenging to meet the increasing energy demands.

Films based on other 2D materials such as black phosphorus have also attracted significant attention recently. The development of black phosphorus-based films is currently limited by their unsatisfying stripping methods and film-forming methods. In contrast, solution-based methods are convenient and cost-effective for the large-scale preparation of MXene-based films,

which is favorable for a wide range of practical applications.[69, 209, 210] As for graphene-based films, a noticeable point for the practical application is the trade-off between the high electrical conductivity and surface functionality. Specifically, rGO films have more surface functional groups but less electrical conductivity compared to graphene films, as we discussed previously. In comparison, $Ti_3C_2T_x$ films feature integrated high electrical conductivity and desirable surface terminations, which is useful for further modifications to meet required properties for target applications. Compared with the intensive studies on graphene, research on $Ti_3C_2T_x$-based films is still in the infancy stage, with many unknowns to be explored. Along with the further investigations on $Ti_3C_2T_x$-based films, distinctive properties and outstanding performances can be achieved. With the continuous inputs from the diverse fields of physics, chemistry and material science, we believe that $Ti_3C_2T_x$-based films hold great potential for technological advances.

References

[1]   Q. Tang; Z. Zhou, *Prog. Mater. Sci.* **2013**, *58*, 1244-1315.

[2] V. M. H. Ng; H. Huang; K. Zhou; P. S. Lee; W. Que; J. Z. Xu; L. B. Kong, *J. Mater. Chem. A* **2017**, *5*, 3039-3068.

[3] L. Li; X. Fu; S. Chen; S. Uzun; A. S. Levitt; C. E. Shuck; W. Han; Y. Gogotsi, *ACS Appl. Mater. Interfaces* **2020**, *12*, 15362-15369.

[4] S. Xu; G. Wei; J. Li; W. Han; Y. Gogotsi, *J. Mater. Chem. A* **2017**, *5*, 17442-17451.

[5] Y. A. Al-Hamadani; B.-M. Jun; M. Yoon; N. Taheri-Qazvini; S. A. Snyder; M. Jang; J. Heo; Y. Yoon, *Chemosphere* **2020**, *254*, 126821.

[6] P. He; M.-S. Cao; Y.-Z. Cai; J.-C. Shu; W.-Q. Cao; J. Yuan, *Carbon* **2020**, *157*, 80-89.

[7] K. S. Novoselov; A. K. Geim; S. V. Morozov; D. Jiang; Y. Zhang; S. V. Dubonos; I. V. Grigorieva; A. A. Firsov, *Science* **2004**, *306*, 666-669.

[8] X. Cai; Y. Luo; B. Liu; H.-M. Cheng, *Chem. Soc. Rev.* **2018**, *47*, 6224-6266.

[9] Y. Dong; Z.-S. Wu; W. Ren; H.-M. Cheng; X. Bao, *Sci. Bull.* **2017**, *62*, 724-740.

[10] M. Naguib; M. Kurtoglu; V. Presser; J. Lu; J. Niu; M. Heon; L. Hultman; Y. Gogotsi; M. W. Barsoum, *Adv. Mater.* **2011**, *23*, 4248-4253.

[11] M. Sokol; V. Natu; S. Kota; M. W. Barsoum, *Trends Chem.* **2019**, *1*, 210-223.

[12] M. Naguib; O. Mashtalir; J. Carle; V. Presser; J. Lu; L. Hultman; Y. Gogotsi; M. W. Barsoum, *ACS Nano* **2012**, *6*, 1322-1331.

[13] M. Alhabeb; K. Maleski; B. Anasori; P. Lelyukh; L. Clark; S. Sin; Y. Gogotsi, *Chem. Mater.* **2017**, *29*, 7633-7644.

[14] J.-C. Lei; X. Zhang; Z. Zhou, *Front. Phys.* **2015**, *10*, 276-286.

[15] B. Anasori; M. R. Lukatskaya; Y. Gogotsi, *Nat. Rev. Mater.* **2017**, *2*, 1-17.

[16] M. Naguib; V. N. Mochalin; M. W. Barsoum; Y. Gogotsi, *Adv. Mater.* **2014**, *26*, 982-982.

[17] Y. Gogotsi; B. Anasori, *ACS Nano* **2019**, *13*, 8491-8494.

[18] Y. Li; H. Shao; Z. Lin; J. Lu; L. Liu; B. Duployer; P. O. Persson; P. Eklund; L. Hultman; M. Li, *Nat. Mater.* **2020**, *19*, 894-899.

[19] M. A. Hope; A. C. Forse; K. J. Griffith; M. R. Lukatskaya; M. Ghidiu; Y. Gogotsi; C. P. Grey, *Phys. Chem. Chem. Phys.* **2016**, *18*, 5099-5102.

[20] K. Hantanasirisakul; Y. Gogotsi, *Adv. Mater.* **2018**, *30*, 1804779.

[21] N. C. Frey; J. Wang; G. I. Vega Bellido; B. Anasori; Y. Gogotsi; V. B. Shenoy, *ACS Nano* **2019**, *13*, 3031-3041.

[22] K. Maleski; V. N. Mochalin; Y. Gogotsi, *Chem. Mater.* **2017**, *29*, 1632-1640.

[23] J. Zhang; N. Kong; S. Uzun; A. Levitt; S. Seyedin; P. A. Lynch; S. Qin; M. Han; W. Yang; J. Liu, *Adv. Mater.* **2020**, *32*, 2001093.

[24] R. Li; L. Zhang; L. Shi; P. Wang, *ACS Nano* **2017**, *11*, 3752-3759.

[25] Y. Liu; G. Yu; G. D. Li; Y. Sun; T. Asefa; W. Chen; X. Zou, *Angew. Chem. Int. Ed.* **2015**, *127*, 10902-10907.

[26] J. Come; M. Naguib; P. Rozier; M. W. Barsoum; Y. Gogotsi; P.-L. Taberna; M. Morcrette; P. Simon, *J. Electrochem. Soc.* **2012**, *159*, A1368.

[27] S. Zhao; X. Meng; K. Zhu; F. Du; G. Chen; Y. Wei; Y. Gogotsi; Y. Gao, *Energy Storage Mater.* **2017**, *8*, 42-48.

[28] J. Hu; B. Xu; C. Ouyang; Y. Zhang; S. A. Yang, *RSC Adv.* **2016**, *6*, 27467-27474.

[29] E. RUDY; C. E. BRUKL, *J. Am. Ceram. Soc.* **1967**, *50*, 265-268.

[30] B. Anasori; Y. Xie; M. Beidaghi; J. Lu; B. C. Hosler; L. Hultman; P. R. Kent; Y. Gogotsi; M. W. Barsoum, *ACS Nano* **2015**, *9*, 9507-9516.

[31] B. Anasori; C. Shi; E. J. Moon; Y. Xie; C. A. Voigt; P. R. Kent; S. J. May; S. J. Billinge; M. W. Barsoum; Y. Gogotsi, *Nanoscale Horiz.* **2016**, *1*, 227-234.

[32] T. S. Mathis; K. Maleski; A. Goad; A. Sarycheva; M. Anayee; A. C. Foucher; K. Hantanasirisakul; C. E. Shuck; E. A. Stach; Y. Gogotsi, *ACS Nano* **2021**, *15*, 6420-6429.

[33] Z. Ling; C. E. Ren; M.-Q. Zhao; J. Yang; J. M. Giammarco; J. Qiu; M. W. Barsoum; Y. Gogotsi, *Proc. Natl. Acad. Sci* **2014**, *111*, 16676-16681.

[34] N. K. Chaudhari; H. Jin; B. Kim; D. San Baek; S. H. Joo; K. Lee, *J. Mater. Chem. A* **2017**, *5*, 24564-24579.

[35] X. Zang; J. Wang; Y. Qin; T. Wang; C. He; Q. Shao; H. Zhu; N. Cao, *Nano-Micro Lett.* **2020**, *12*, 1-24.

[36] J. Zhou; J. Yu; L. Shi; Z. Wang; H. Liu; B. Yang; C. Li; C. Zhu; J. Xu, *Small* **2018**, *14*, 1803786.

[37] M.-S. Cao; Y.-Z. Cai; P. He; J.-C. Shu; W.-Q. Cao; J. Yuan, *Chem. Eng. J.* **2019**, *359*, 1265-1302.

[38] A. Sarycheva; A. Polemi; Y. Liu; K. Dandekar; B. Anasori; Y. Gogotsi, *Sci. Adv.* **2018**, *4*, eaau0920.

[39] L. Huang; L. Ai; M. Wang; J. Jiang; S. Wang, *Int. J. Hydrog. Energy* **2019**, *44*, 965-976.

[40] Y. Ma; N. Liu; L. Li; X. Hu; Z. Zou; J. Wang; S. Luo; Y. Gao, *Nat. Commun.* **2017**, *8*, 1-8.

[41] T. Liu; X. Liu; N. Graham; W. Yu; K. Sun, *J. Membr. Sci.* **2020**, *593*, 117431.

[42] L. Yu; L. Hu; B. Anasori; Y.-T. Liu; Q. Zhu; P. Zhang; Y. Gogotsi; B. Xu, *ACS Energy Lett.* **2018**, *3*, 1597-1603.

[43] J. Pang; R. G. Mendes; A. Bachmatiuk; L. Zhao; H. Q. Ta; T. Gemming; H. Liu; Z. Liu; M. H. Rummeli, *Chem. Soc. Rev.* **2019**, *48*, 72-133.

[44] Y. Tian; Y. An; C. Wei; B. Xi; S. Xiong; J. Feng; Y. Qian, *ACS Nano* **2019**, *13*, 11676-11685.

[45] S. J. Kim; M. Naguib; M. Zhao; C. Zhang; H.-T. Jung; M. W. Barsoum; Y. Gogotsi, *Electrochim. Acta* **2015**, *163*, 246-251.

[46] H. Tang; W. Li; L. Pan; K. Tu; F. Du; T. Qiu; J. Yang; C. P. Cullen; N. McEvoy; C. Zhang, *Adv. Funct. Mater.* **2019**, *29*, 1901907.

[47] H. Huang; H. Su; H. Zhang; L. Xu; X. Chu; C. Hu; H. Liu; N. Chen; F. Liu; W. Deng, *Adv. Electron. Mater.* **2018**, *4*, 1800179.

[48] S. Xu; G. Wei; J. Li; Y. Ji; N. Klyui; V. Izotov; W. Han, *Chem. Eng. J.* **2017**, *317*, 1026-1036.

[49] L. Peng; Z. Fang; Y. Zhu; C. Yan; G. Yu, *Adv. Energy Mater.* **2018**, *8*, 1702179.

[50] Y. Wang; Y. Li; Z. Qiu; X. Wu; P. Zhou; T. Zhou; J. Zhao; Z. Miao; J. Zhou; S. Zhuo, *J. Mater. Chem. A* **2018**, *6*, 11189-11197.

[51] F. Bu; I. Shakir; Y. Xu, *Adv. Mater. Interfaces* **2018**, *5*, 1800468.

[52] Q. Yun; Q. Lu; X. Zhang; C. Tan; H. Zhang, *Angew. Chem. Int. Ed.* **2018**, *57*, 626-646.

[53] F. Bu; M. M. Zagho; Y. Ibrahim; B. Ma; A. Elzatahry; D. Zhao, *Nano Today* **2019**, 100803.

[54] Q. Zhao; Q. Zhu; J. Miao; P. Zhang; P. Wan; L. He; B. Xu, *Small* **2019**, *15*, 1904293.

[55] B. C. Wyatt; A. Rosenkranz; B. Anasori, *Adv. Mater.* **2021**, *33*, 2007973.

[56] Y. Wang; X. Wang; X. Li; Y. Bai; H. Xiao; Y. Liu; R. Liu; G. Yuan, *Adv. Funct. Mater.* **2019**, *29*, 1900326.

[57] H.-J. Zhang; K.-X. Wang; X.-Y. Wu; Y.-M. Jiang; Y.-B. Zhai; C. Wang; X. Wei; J.-S. Chen, *Adv. Funct. Mater.* **2014**, *24*, 3399-3404.

[58] G. Ying; A. D. Dillon; A. T. Fafarman; M. W. Barsoum, *Mater. Res. Lett.* **2017**, *5*, 391-398.

[59] S. Zhao; C. Chen; X. Zhao; X. Chu; F. Du; G. Chen; Y. Gogotsi; Y. Gao; Y. Dall'Agnese, *Adv. Funct. Mater.* **2020**, *30*, 2000815.

[60] J. Halim; I. Persson; E. J. Moon; P. Kühne; V. Darakchieva; P. O. Å. Persson; P. Eklund; J. Rosen; M. W. Barsoum, *J. Phys. Condens. Matter* **2019**, *31*, 165301.

[61] G. Ying; S. Kota; A. D. Dillon; A. T. Fafarman; M. W. Barsoum, *Flatchem* **2018**, *8*, 25-30.

[62] F. Shahzad; M. Alhabeb; C. B. Hatter; B. Anasori; S. M. Hong; C. M. Koo; Y. Gogotsi, *Science* **2016**, *353*, 1137-1140.

[63] V. Natu; J. L. Hart; M. Sokol; H. Chiang; M. L. Taheri; M. W. Barsoum, *Angew. Chem. Int. Ed.* **2019**, *58*, 12655-12660.

[64] Z. Fan; Y. Wang; Z. Xie; X. Xu; Y. Yuan; Z. Cheng; Y. Liu, *Nanoscale* **2018**, *10*, 9642-9652.

[65] J. L. Hart; K. Hantanasirisakul; A. C. Lang; B. Anasori; D. Pinto; Y. Pivak; J. T. van Omme; S. J. May; Y. Gogotsi; M. L. Taheri, *Nat. Commun.* **2019**, *10*, 1-10.

[66] M. R. Lukatskaya; S. Kota; Z. Lin; M.-Q. Zhao; N. Shpigel; M. D. Levi; J. Halim; P.-L. Taberna; M. W. Barsoum; P. Simon, *Nat. Energy* **2017**, *2*, 17105.

[67] W. Zheng; J. Halim; A. El Ghazaly; A. S. Etman; E. N. Tseng; P. O. Å. Persson; J. Rosen; M. W. Barsoum, *Adv. Sci.* **2021**, *8*, 2003656.

[68] M. Mariano; O. Mashtalir; F. Q. Antonio; W.-H. Ryu; B. Deng; F. Xia; Y. Gogotsi; A. D. Taylor, *Nanoscale* **2016**, *8*, 16371-16378.

[69] J. Zhang; N. Kong; S. Uzun; A. Levitt; S. Seyedin; P. A. Lynch; S. Qin; M. Han; W. Yang; J. Liu; X. Wang; Y. Gogotsi; J. M. Razal, *Adv. Mater.* **2020**, *32*, 2001093.

[70] H. Chen; Y. Wen; Y. Qi; Q. Zhao; L. Qu; C. Li, *Adv. Funct. Mater.* **2020**, *30*, 1906996.

[71] Z. Fan; H. He; J. Yu; L. Liu; Y. Liu; Z. Xie, *ACS Appl. Energy Mater.* **2020**, *3*, 8171-8178.

[72] Z. Liu; Y. Zhang; H.-B. Zhang; Y. Dai; J. Liu; X. Li; Z.-Z. Yu, *J. Mater. Chem. C* **2020**, *8*, 1673-1678.

[73] W.-T. Cao; F.-F. Chen; Y.-J. Zhu; Y.-G. Zhang; Y.-Y. Jiang; M.-G. Ma; F. Chen, *ACS Nano* **2018**, *12*, 4583-4593.

[74] T. Zhou; C. Wu; Y. Wang; A. P. Tomsia; M. Li; E. Saiz; S. Fang; R. H. Baughman; L. Jiang; Q. Cheng, *Nat. Commun.* **2020**, *11*, 1-11.

[75] W. Yang; J.-J. Liu; L.-L. Wang; W. Wang; A. C. Y. Yuen; S. Peng; B. Yu; H.-D. Lu; G. H. Yeoh; C.-H. Wang, *Compos. B. Eng.* **2020**, *188*, 107875.

[76] C. Lei; Y. Zhang; D. Liu; K. Wu; Q. Fu, *ACS Appl. Mater. Interfaces* **2020**, *12*, 26485-26495.

[77] X. Xie; C. Chen; N. Zhang; Z.-R. Tang; J. Jiang; Y.-J. Xu, *Nat. Sustain.* **2019**, *2*, 856-862.

[78] J. Liu; H. B. Zhang; R. Sun; Y. Liu; Z. Liu; A. Zhou; Z. Z. Yu, *Adv. Mater.* **2017**, *29*, 1702367.

[79] F. Ran; T. Wang; S. Chen; Y. Liu; L. Shao, *Appl. Surf. Sci.* **2020**, *511*, 145627.

[80] Z. Fan; Y. Wang; Z. Xie; D. Wang; Y. Yuan; H. Kang; B. Su; Z. Cheng; Y. Liu, *Adv. Sci.* **2018**, *5*, 1800750.

[81] C. E. Ren; M. Q. Zhao; T. Makaryan; J. Halim; M. Boota; S. Kota; B. Anasori; M. W. Barsoum; Y. Gogotsi, *ChemElectroChem* **2016**, *3*, 689-693.

[82] Q. Jiang; Y. Lei; H. Liang; K. Xi; C. Xia; H. N. Alshareef, *Energy Storage Mater.* **2020**, *27*, 78-95.

[83] Z. Ma; X. Zhou; W. Deng; D. Lei; Z. Liu, *ACS Appl. Mater. Interfaces* **2018**, *10*, 3634-3643.

[84] Y. Wang; Y. Chen; S. D. Lacey; L. Xu; H. Xie; T. Li; V. A. Danner; L. Hu, *Mater. Today* **2018**, *21*, 186-192.

[85] Y. Liu; M. Yang; K. Pang; F. Wang; Z. Xu; W. Gao; C. Gao, *Carbon* **2020**, *156*, 205-211.

[86] A. Lipatov; M. Alhabeb; M. R. Lukatskaya; A. Boson; Y. Gogotsi; A. Sinitskii, *Adv. Electron. Mater.* **2016**, *2*, 1600255.

[87] X. Sang; Y. Xie; M.-W. Lin; M. Alhabeb; K. L. Van Aken; Y. Gogotsi; P. R. Kent; K. Xiao; R. R. Unocic, *ACS Nano* **2016**, *10*, 9193-9200.

[88] M. Ghidiu; M. R. Lukatskaya; M.-Q. Zhao; Y. Gogotsi; M. W. Barsoum, *Nature* **2014**, *516*, 78-81.

[89] J. N. Coleman; M. Lotya; A. O'Neill; S. D. Bergin; P. J. King; U. Khan; K. Young; A. Gaucher; S. De; R. J. Smith, *Science* **2011**, *331*, 568-571.

[90] M. Ashton; K. Mathew; R. G. Hennig; S. B. Sinnott, *J. Phys. Chem. C* **2016**, *120*, 3550-3556.

[91] S. Luo; S. Patole; S. Anwer; B. Li; T. Delclos; O. Gogotsi; V. Zahorodna; V. Balitskyi; K. Liao, *Nanotechnol.* **2020**, *31*, 395704.

[92] T. Hu; M. Hu; Z. Li; H. Zhang; C. Zhang; J. Wang; X. Wang, *Phys. Chem. Chem. Phys.* **2016**, *18*, 20256-20260.

[93] M. Boota; B. Anasori; C. Voigt; M. Q. Zhao; M. W. Barsoum; Y. Gogotsi, *Adv. Mater.* **2016**, *28*, 1517-1522.

[94] A. VahidMohammadi; J. Moncada; H. Chen; E. Kayali; J. Orangi; C. A. Carrero; M. Beidaghi, *J. Mater. Chem. A* **2018**, *6*, 22123-22133.

[95] J. Yang; W. Bao; P. Jaumaux; S. Zhang; C. Wang; G. Wang, *Adv. Mater. Interfaces* **2019**, *6*, 1802004.

[96] M. Q. Zhao; X. Xie; C. E. Ren; T. Makaryan; B. Anasori; G. Wang; Y. Gogotsi, *Adv. Mater.* **2017**, *29*, 1702410.

[97] J. Wang; Y. Liu; Z. Cheng; Z. Xie; L. Yin; W. Wang; Y. Song; H. Zhang; Y. Wang; Z. Fan, *Angew. Chem. Int. Ed.* **2020**, *132*, 14133-14137.

[98] C. Zhang; M. P. Kremer; A. Seral-Ascaso; S. H. Park; N. McEvoy; B. Anasori; Y. Gogotsi; V. Nicolosi, *Adv. Funct. Mater.* **2018**, *28*, 1705506.

[99] T. Habib; X. Zhao; S. A. Shah; Y. Chen; W. Sun; H. An; J. L. Lutkenhaus; M. Radovic; M. J. Green, *NPJ 2D Mater. Appl.* **2019**, *3*, 1-6.

[100] O. Mashtalir; K. M. Cook; V. N. Mochalin; M. Crowe; M. W. Barsoum; Y. Gogotsi, *J. Mater. Chem. A* **2014**, *2*, 14334-14338.

[101] C. J. Zhang; S. Pinilla; N. McEvoy; C. P. Cullen; B. Anasori; E. Long; S.-H. Park; A. s. Seral-Ascaso; A. Shmeliov; D. Krishnan, *Chem. Mater.* **2017**, *29*, 4848-4856.

[102] X. Zhao; Z. Wang; J. Dong; T. Huang; Q. Zhang; L. Zhang, *J. Power Sources* **2020**, *470*, 228356.

[103] O. Mashtalir; M. Naguib; V. N. Mochalin; Y. Dall'Agnese; M. Heon; M. W. Barsoum; Y. Gogotsi, *Nat. Commun.* **2013**, *4*, 1-7.

[104] C. E. Shuck; Y. Gogotsi, *Chem. Eng. J.* **2020**, *401*, 125786.

[105] B. Yang; M. Zhang; Z. Lu; J. Tan; J. Luo; S. Song; X. Ding; L. Wang; P. Lu; Q. Zhang, *Carbohydr. Polym.* **2019**, *208*, 372-381.

[106] H. Wang; Y. Wu; X. Yuan; G. Zeng; J. Zhou; X. Wang; J. W. Chew, *Adv. Mater.* **2018**, *30*, 1704561.

[107] Y. Tian; Y. An; S. Xiong; J. Feng; Y. Qian, *J. Mater. Chem. A* **2019**, *7*, 9716-9725.

[108] K. Hantanasirisakul; M. Q. Zhao; P. Urbankowski; J. Halim; B. Anasori; S. Kota; C. E. Ren; M. W. Barsoum; Y. Gogotsi, *Adv. Electron. Mater.* **2016**, *2*, 1600050.

[109] F. Xie; F. Jia; L. Zhuo; Z. Lu; L. Si; J. Huang; M. Zhang; Q. Ma, *Nanoscale* **2019**, *11*, 23382-23391.

[110] G. Liu; J. Shen; Q. Liu; G. Liu; J. Xiong; J. Yang; W. Jin, *J. Membr. Sci.* **2018**, *548*, 548-558.

[111] J. Wang; P. Chen; B. Shi; W. Guo; M. Jaroniec; S. Z. Qiao, *Angew. Chem. Int. Ed.* **2018**, *57*, 6814-6818.

[112] S. Huang; V. N. Mochalin, *Inorg. Chem.* **2019**, *58*, 1958-1966.

[113] J. Shen; G. Liu; Y. Ji; Q. Liu; L. Cheng; K. Guan; M. Zhang; G. Liu; J. Xiong; J. Yang, *Adv. Funct. Mater.* **2018**, *28*, 1801511.

[114] L. H. Karlsson; J. Birch; J. Halim; M. W. Barsoum; P. O. Persson, *Nano Lett.* **2015**, *15*, 4955-4960.

[115] S. Yamamoto; H. Bluhm; K. Andersson; G. Ketteler; H. Ogasawara; M. Salmeron; A. Nilsson, *J. Phys. Condens. Matter* **2008**, *20*, 184025.

[116] X. Gao; J. Jang; S. Nagase, *J. Phys. Chem. C* **2010**, *114*, 832-842.

[117] X. Xie; M.-Q. Zhao; B. Anasori; K. Maleski; C. E. Ren; J. Li; B. W. Byles; E. Pomerantseva; G. Wang; Y. Gogotsi, *Nano Energy* **2016**, *26*, 513-523.

[118] Z. Wang; Q. Tu; S. Zheng; J. J. Urban; S. Li; B. Mi, *Nano Lett.* **2017**, *17*, 7289-7298.

[119] R. Joshi; P. Carbone; F.-C. Wang; V. G. Kravets; Y. Su; I. V. Grigorieva; H. Wu; A. K. Geim; R. R. Nair, *Science* **2014**, *343*, 752-754.

[120] L. Ding; Y. Wei; L. Li; T. Zhang; H. Wang; J. Xue; L.-X. Ding; S. Wang; J. Caro; Y. Gogotsi, *Nat. Commun.* **2018**, *9*, 1-7.

[121] L. M. Robeson, *J. Membr. Sci.* **2008**, *320*, 390-400.

[122] C. E. Ren; K. B. Hatzell; M. Alhabeb; Z. Ling; K. A. Mahmoud; Y. Gogotsi, *J. Phys. Chem. Lett.* **2015**, *6*, 4026-4031.

[123] P. Collini; S. Kota; A. D. Dillon; M. W. Barsoum; A. T. Fafarman, *J. Electrochem. Soc.* **2017**, *164*, D573-D580.

[124] M. Q. Zhao; C. E. Ren; Z. Ling; M. R. Lukatskaya; C. Zhang; K. L. Van Aken; M. W. Barsoum; Y. Gogotsi, *Adv. Mater.* **2015**, *27*, 339-345.

[125] S. Abdolhosseinzadeh; J. Heier; C. Zhang, *ChemElectroChem* **2021**,

[126] S. Abdolhosseinzadeh; X. Jiang; H. Zhang; J. Qiu; C. J. Zhang, *Mater. Today* **2021**,

[127] B. Akuzum; K. Maleski; B. Anasori; P. Lelyukh; N. J. Alvarez; E. C. Kumbur; Y. Gogotsi, *ACS Nano* **2018**, *12*, 2685-2694.

[128] S. Naficy; R. Jalili; S. H. Aboutalebi; R. A. Gorkin III; K. Konstantinov; P. C. Innis; G. M. Spinks; P. Poulin; G. G. Wallace, *Mater. Horiz* **2014**, *1*, 326-331.

[129] C. Zhang; B. Anasori; A. Seral-Ascaso; S. H. Park; N. McEvoy; A. Shmeliov; G. S. Duesberg; J. N. Coleman; Y. Gogotsi; V. Nicolosi, *Adv. Mater.* **2017**, *29*, 1702678.

[130] Q. Li; H. Li; Q. Xia; Z. Hu; Y. Zhu; S. Yan; C. Ge; Q. Zhang; X. Wang; X. Shang, *Nat. Mater.* **2021**, *20*, 76-83.

[131] H. Li; Z. Hu; Q. Xia; H. Zhang; Z. Li; H. Wang; X. Li; F. Zuo; F. Zhang; X. Wang, *Adv. Mater.* **2021**, *33*, 2006629.

[132] D. Xu; M. Liang; S. Qi; W. Sun; L.-P. Lv; F.-H. Du; B. Wang; S. Chen; Y. Wang; Y. Yu, *ACS Nano* **2021**, *15*, 47-80.

[133] C. Guo; J. Yang; Z. Cui; S. Qi; Q. Peng; W. Sun; L.-P. Lv; Y. Xu; Y. Wang; S. Chen, *J. Energy Chem.* **2021**,

[134] Q. Zhao; Q. Zhu; J. Miao; P. Zhang; P. Wan; L. He; B. Xu, *Small* **2019**, 1904293.

[135] M. Xu; S. Lei; J. Qi; Q. Dou; L. Liu; Y. Lu; Q. Huang; S. Shi; X. Yan, *ACS Nano* **2018**, *12*, 3733-3740.

[136] W. Zheng; P. Zhang; J. Chen; W. Tian; Y. Zhang; Z. Sun, *J. Mater. Chem. A* **2018**, *6*, 3543-3551.

[137] C. Chen; M. Boota; X. Xie; M. Zhao; B. Anasori; C. E. Ren; L. Miao; J. Jiang; Y. Gogotsi, *J. Mater. Chem. A* **2017**, *5*, 5260-5265.

[138] J. Yan; C. E. Ren; K. Maleski; C. B. Hatter; B. Anasori; P. Urbankowski; A. Sarycheva; Y. Gogotsi, *Adv. Funct. Mater.* **2017**, *27*, 1701264.

[139] Y. Tian; Y. An; J. Feng, *ACS Appl. Mater. Interfaces* **2019**, *11*, 10004-10011.

[140] X. Wang; S. Kajiyama; H. Iinuma; E. Hosono; S. Oro; I. Moriguchi; M. Okubo; A. Yamada, *Nat. Commun.* **2015**, *6*, 1-6.

[141] X. Wu; Z. Wang; M. Yu; L. Xiu; J. Qiu, *Adv. Mater.* **2017**, *29*, 1607017.

[142] M. R. Lukatskaya; S. M. Bak; X. Yu; X. Q. Yang; M. W. Barsoum; Y. Gogotsi, *Adv. Energy Mater.* **2015**, *5*, 1500589.

[143] Y. Zhu; K. Rajouâ; S. Le Vot; O. Fontaine; P. Simon; F. Favier, *Nano Energy* **2020**, *73*, 104734.

[144] Q. Jiang; N. Kurra; M. Alhabeb; Y. Gogotsi; H. N. Alshareef, *Adv. Energy Mater.* **2018**, *8*, 1703043.

[145] X. Zhang; Y. Liu; S. Dong; J. Yang; X. Liu, *Electrochim. Acta* **2019**, *294*, 233-239.

[146] M. Hu; Z. Li; H. Zhang; T. Hu; C. Zhang; Z. Wu; X. Wang, *Chem. Commun.* **2015**, *51*, 13531-13533.

[147] D. Xiong; X. Li; Z. Bai; S. Lu, *Small* **2018**, *14*, 1703419.

[148] P. Liu; W. Ding; J. Liu; L. Shen; F. Jiang; P. Liu; Z. Zhu; G. Zhang; C. Liu; J. Xu, *J. Alloys Compd.* **2020**, *829*, 154634.

[149] S. Liu; K. He; X. Wu; X. Luo; B. Li, *RSC Adv.* **2015**, *5*, 87266-87276.

[150] Y. Xie; M. Naguib; V. N. Mochalin; M. W. Barsoum; Y. Gogotsi; X. Yu; K.-W. Nam; X.-Q. Yang; A. I. Kolesnikov; P. R. Kent, *J. Am. Chem. Soc.* **2014**, *136*, 6385-6394.

[151] Q. Peng; J. Guo; Q. Zhang; J. Xiang; B. Liu; A. Zhou; R. Liu; Y. Tian, *J. Am. Chem. Soc.* **2014**, *136*, 4113-4116.

[152] M. Beidaghi; Y. Gogotsi, *Energy Environ. Sci.* **2014**, *7*, 867-884.

[153] Y.-Y. Peng; B. Akuzum; N. Kurra; M.-Q. Zhao; M. Alhabeb; B. Anasori; E. C. Kumbur; H. N. Alshareef; M.-D. Ger; Y. Gogotsi, *Energy Environ. Sci.* **2016**, *9*, 2847-2854.

[154] N. Kurra; B. Ahmed; Y. Gogotsi; H. N. Alshareef, *Adv. Energy Mater.* **2016**, *6*, 1601372.

[155] H. Hu; Z. Bai; B. Niu; M. Wu; T. Hua, *J. Mater. Chem. A* **2018**, *6*, 14876-14884.

[156] Y. Yang; S. Umrao; S. Lai; S. Lee, *J. Phys. Chem. Lett.* **2017**, *8*, 859-865.

[157] H. A. Becerril; J. Mao; Z. Liu; R. M. Stoltenberg; Z. Bao; Y. Chen, *ACS Nano* **2008**, *2*, 463-470.

[158] J. Kim; J. W. Lim; F. M. Mota; J.-E. Lee; R. Boppella; K. Y. Lim; K. Kim; W. K. Choi; D. H. Kim, *Nanoscale* **2016**, *8*, 18938-18944.

[159] B. Ahmed; D. H. Anjum; M. N. Hedhili; Y. Gogotsi; H. N. Alshareef, *Nanoscale* **2016**, *8*, 7580-7587.

[160] M. R. Lukatskaya; O. Mashtalir; C. E. Ren; Y. Dall'Agnese; P. Rozier; P. L. Taberna; M. Naguib; P. Simon; M. W. Barsoum; Y. Gogotsi, *Science* **2013**, *341*, 1502-1505.

[161] R. P. Pandey; K. Rasool; V. E. Madhavan; B. Aïssa; Y. Gogotsi; K. A. Mahmoud, *J. Mater. Chem. A* **2018**, *6*, 3522-3533.

[162] L. Ding; Y. Wei; Y. Wang; H. Chen; J. Caro; H. Wang, *Angew. Chem. Int. Ed.* **2017**, *56*, 1825-1829.

[163] K. Raagulan; B. M. Kim; K. Y. Chai, *Nanomaterials* **2020**, *10*, 702.

[164] Y. Xu; Y. S. Ang; L. Wu; L. K. Ang, *Nanomaterials* **2019**, *9*, 165.

[165] Y. Ma; Y. Yue; H. Zhang; F. Cheng; W. Zhao; J. Rao; S. Luo; J. Wang; X. Jiang; Z. Liu, *ACS Nano* **2018**, *12*, 3209-3216.

[166] B. Shen; W. Zhai; W. Zheng, *Adv. Funct. Mater.* **2014**, *24*, 4542-4548.

[167] S. Kim; J.-S. Oh; M.-G. Kim; W. Jang; M. Wang; Y. Kim; H. W. Seo; Y. C. Kim; J.-H. Lee; Y. Lee, *ACS Appl. Mater. Interfaces* **2014**, *6*, 17647-17653.

[168] A. A. Barba; G. Lamberti; M. d'Amore; D. Acierno, *Polym. Bull.* **2006**, *57*, 587-593.

[169] L. Gao; C. Li; W. Huang; S. Mei; H. Lin; Q. Ou; Y. Zhang; J. Guo; F. Zhang; S. Xu, *Chem. Mater.* **2020**, *32*, 1703-1747.

[170] F. Liu; Y. Li; S. Hao; Y. Cheng; Y. Zhan; C. Zhang; Y. Meng; Q. Xie; H. Xia, *Carbohydr. Polym.* **2020**, *243*, 116467.

[171] Y.-J. Wan; X.-M. Li; P.-L. Zhu; R. Sun; C.-P. Wong; W.-H. Liao, *Compos. Part A Appl. Sci. Manuf.* **2020**, *130*, 105764.

[172] B. Qu; J. r. Li; H. n. Xiao; B. h. He; L. y. Qian, *Polym. Compos.* **2016**, *37*, 3050-3056.

[173] Z. Zhou; J. Liu; X. Zhang; D. Tian; Z. Zhan; C. Lu, *Adv. Mater. Interfaces* **2019**, *6*, 1802040.

[174] W. Chen; L.-X. Liu; H.-B. Zhang; Z.-Z. Yu, *ACS Nano* **2020**, *14*, 16643-16653.

[175] E. Lee; A. VahidMohammadi; B. C. Prorok; Y. S. Yoon; M. Beidaghi; D.-J. Kim, *ACS Appl. Mater. Interfaces* **2017**, *9*, 37184-37190.

[176] F. K. Perkins; A. L. Friedman; E. Cobas; P. Campbell; G. Jernigan; B. T. Jonker, *Nano Lett.* **2013**, *13*, 668-673.

[177] H. Zhang; A. Kulkarni; H. Kim; D. Woo; Y.-J. Kim; B. H. Hong; J.-B. Choi; T. Kim, *J. Nanosci. Nanotechnol.* **2011**, *11*, 5939-5943.

[178] H. An; T. Habib; S. Shah; H. Gao; M. Radovic; M. J. Green; J. L. Lutkenhaus, *Sci. Adv.* **2018**, *4*, eaaq0118.

[179] Y. Yang; N. Sun; Z. Wen; P. Cheng; H. Zheng; H. Shao; Y. Xia; C. Chen; H. Lan; X. Xie, *ACS Nano* **2018**, *12*, 2027-2034.

[180] R. Wen; J. Guo; A. Yu; K. Zhang; J. Kou; Y. Zhu; Y. Zhang; B.-W. Li; J. Zhai, *Nano Energy* **2018**, *50*, 140-147.

[181] H.-W. Park; N. D. Huynh; W. Kim; C. Lee; Y. Nam; S. Lee; K.-B. Chung; D. Choi, *Nano Energy* **2018**, *50*, 9-15.

[182] C. Jiang; C. Wu; X. Li; Y. Yao; L. Lan; F. Zhao; Z. Ye; Y. Ying; J. Ping, *Nano Energy* **2019**, *59*, 268-276.

[183] V. S. Sivasankarapillai; A. K. Somakumar; J. Joseph; S. Nikazar; A. Rahdar; G. Z. Kyzas, *Nano-Struct. Nano-Objects* **2020**, *22*, 100457.

[184] K. Huang; Z. Li; J. Lin; G. Han; P. Huang, *Chem. Soc. Rev.* **2018**, *47*, 5109-5124.

[185] H. Lin; Y. Chen; J. Shi, *Adv. Sci.* **2018**, *5*, 1800518.

[186] B. Xu; M. Zhu; W. Zhang; X. Zhen; Z. Pei; Q. Xue; C. Zhi; P. Shi, *Adv. Mater.* **2016**, *28*, 3333-3339.

[187] D. Xu; Z. Li; L. Li; J. Wang, *Adv. Funct. Mater.* **2020**, *30*, 2000712.

[188] J. Zhao; Y. Yang; C. Yang; Y. Tian; Y. Han; J. Liu; X. Yin; W. Que, *J. Mater. Chem. A* **2018**, *6*, 16196-16204.

[189] L. Zong; H. Wu; H. Lin; Y. Chen, *Nano Res.* **2018**, *11*, 4149-4168.

[190] W.-T. Cao; W. Feng; Y.-Y. Jiang; C. Ma; Z.-F. Zhou; M.-G. Ma; Y. Chen; F. Chen, *Mater. Horiz* **2019**, *6*, 1057-1065.

[191] R. Liu; W. Li, *ACS omega* **2018**, *3*, 2609-2617.

[192] W. Liu; Y. Cheng; N. Liu; Y. Yue; D. Lei; T. Su; M. Zhu; Z. Zhang; W. Zeng; H. Guo, *Chem. Eng. J.* **2021**, *417*, 129288.

[193] C. M. Lopes; M. I. Felisberti, *Polym. Test.* **2004**, *23*, 637-643.

[194] M. Fei; R. Lin; Y. Deng; H. Xian; R. Bian; X. Zhang; J. Cheng; C. Xu; D. Cai, *Nanotechnol.* **2017**, *29*, 035403.

[195] C. Cui; R. Guo; H. Xiao; E. Ren; Q. Song; C. Xiang; X. Lai; J. Lan; S. Jiang, *Appl. Surf. Sci.* **2020**, *505*, 144595.

[196] Y. Zhuang; Y. Liu; X. Meng, *Appl. Surf. Sci.* **2019**, *496*, 143647.

[197] H. Zou; B. He; P. Kuang; J. Yu; K. Fan, *ACS Appl. Mater. Interfaces* **2018**, *10*, 22311-22319.

[198] L. Xiu; Z. Wang; M. Yu; X. Wu; J. Qiu, *ACS Nano* **2018**, *12*, 8017-8028.

[199] H. C. Fu; V. Ramalingam; H. Kim; C. H. Lin; X. Fang; H. N. Alshareef; J. H. He, *Adv. Energy Mater.* **2019**, *9*, 1900180.

[200] Y. Nie; J. Huang; S. Ma; Z. Li; Y. Shi; X. Yang; X. Fang; J. Zeng; P. Bi; J. Qi, *Appl. Surf. Sci.* **2020**, *527*, 146915.

[201] X. Chen; Z. Kong; N. Li; X. Zhao; C. Sun, *Phys. Chem. Chem. Phys.* **2016**, *18*, 32937-32943.

[202] Z. Zhang; S. Yang; P. Zhang; J. Zhang; G. Chen; X. Feng, *Nat. Commun.* **2019**, *10*, 1-9.

[203] L. Verger; V. Natu; M. Ghidiu; M. W. Barsoum, *J. Phys. Chem. C* **2019**, *123*, 20044-20050.

[204] Z. Lu; Y. Wei; J. Deng; L. Ding; Z.-K. Li; H. Wang, *ACS Nano* **2019**, *13*, 10535-10544.

[205] X. Xie; Z. Wu; N. Zhang, *Chin Chem Lett* **2020**, *31*, 1014-1017.

[206] K. H. Thebo; X. Qian; Q. Zhang; L. Chen; H.-M. Cheng; W. Ren, *Nat. Commun.* **2018**, *9*, 1-8.

[207] Y. Long; K. Wang; G. Xiang; K. Song; G. Zhou; X. Wang, *Adv. Mater.* **2017**, *29*, 1606093.

[208] J. Abraham; K. S. Vasu; C. D. Williams; K. Gopinadhan; Y. Su; C. T. Cherian; J. Dix; E. Prestat; S. J. Haigh; I. V. Grigorieva, *Nat. Nanotechnol.* **2017**, *12*, 546.

[209] Z. Zhao; S. Wang; F. Wan; Z. Tie; Z. Niu, *Adv. Funct. Mater.* **2021**, 2101302.

[210] J. H. Kim; G. S. Park; Y.-J. Kim; E. Choi; J. Kang; O. Kwon; S. J. Kim; J. H. Cho; D. W. Kim, *ACS Nano* **2021**, *15*, 8860-8869.

The table of contents entry:

Assembling $Ti_3C_2T_x$ nanosheets into films with well-defined microstructures and unique surface properties creates attractive physicochemical properties favorable for device design, which has emerged as a prevailing paradigm and expanded the scopes in functional film materials. This review provides a series of optimizing strategies about the competitive features of $Ti_3C_2T_x$-based films and its applications. In addition, we cast a personal prospect on the future development of $Ti_3C_2T_x$-based films.

Guohao Li, Brian C. Wyatt, Fei Song, Changqiang Yu, Zhenjun Wu, Xiuqiang Xie*, Babak Anasori*, Nan Zhang*

Two-Dimensional Titanium Carbide (MXene) based Films: Expanding the Frontier of Functional Film Materials

TOC figure